

1   Aerosol radiative effects in the ultraviolet, visible, and near-infrared spectral ranges using long-term  
2   aerosol data series over the Iberian Peninsula

3

4   D. Mateos<sup>1,2</sup>, M. Antón<sup>1</sup>, C. Toledano<sup>2</sup>, V. E. Cachorro<sup>2</sup>, L. Alados-Arboledas<sup>3,4</sup>, M. Sorribas<sup>3,4,5</sup>,  
5   M.J. Costa<sup>6</sup>, J.M. Baldasano<sup>7</sup>.

6   1. Departamento de Física, Universidad de Extremadura, Badajoz, Spain

7   2. Grupo de Óptica Atmosférica, Universidad de Valladolid, Valladolid, Spain

8   3. Departamento de Física Aplicada, Universidad de Granada, Granada, Spain

9   4. Andalusian Institute for Earth System Research, Universidad de Granada, Granada, Spain

10   5. Estación de Sondeos Atmosféricos El Arenosillo, INTA, Huelva, Spain

11   6. Évora Geophysics Centre and Dep. Physics, University of Évora, Évora, Portugal

12   7. Universidad Politécnica de Cataluña, Barcelona, Spain

13

14   Corresponding author: D. Mateos, Grupo de Óptica Atmosférica, Universidad de Valladolid, Paseo

15   Belén 7, 47011, Valladolid, Spain. E-mail: mateos@goa.uva.es

16

17

18

19

20 **Abstract**

21 A better understanding of the aerosol radiative properties is a crucial challenge for climate change  
22 studies. This study aims at providing a complete characterization of aerosol radiative effects in  
23 different spectral ranges within the shortwave (SW) solar spectrum. For this purpose, long-term  
24 datasets of aerosol properties from six AERONET stations located in the Iberian Peninsula  
25 (Southwestern Europe) have been analyzed in terms of climatological characterization and inter-  
26 annual changes. Aerosol information was used as input to the libRadtran model in order to  
27 determine the aerosol radiative effect (ARE) at the surface in the ultraviolet ( $ARE_{UV}$ ), visible  
28 ( $ARE_{VIS}$ ), near-infrared ( $ARE_{NIR}$ ), and the entire SW range ( $ARE_{SW}$ ) under cloud-free conditions.  
29 Over the whole Iberian Peninsula, yearly aerosol radiative effects in the different spectral ranges  
30 were found to be:  $-1.1 < ARE_{UV} < -0.7$ ,  $-5.7 < ARE_{VIS} < -3.5$ ,  $-2.6 < ARE_{NIR} < -1.6$ , and  $-8.8 <$   
31  $ARE_{SW} < -5.7$  (in  $W m^{-2}$ ). Monthly means of ARE showed a seasonal pattern with larger values in  
32 spring and summer. The aerosol forcing efficiency (AFE), ARE per unit of aerosol optical depth,  
33 has also been evaluated in the four spectral ranges. AFE exhibited a dependence on single scattering  
34 albedo and as well as a weaker one on the Ångström exponent. AFE is larger (in absolute value) for  
35 small and absorbing particles. The contributions of the UV, VIS, and NIR ranges to the SW  
36 efficiency varied with the aerosol types. The predominant aerosol size determined the fractions  
37  $AFE_{VIS}/AFE_{SW}$  and  $AFE_{NIR}/AFE_{SW}$ . The  $AFE_{VIS}$  was the dominant contributor for all aerosol types,  
38 although non-absorbing large particles caused more even contribution of VIS and NIR intervals.  
39 The  $AFE_{UV}/AFE_{SW}$  ratio showed a higher value in case of absorbing fine particles.

40

41

42 **1. Introduction**

43 Atmospheric aerosol particles can absorb and scatter part of the total amount of solar radiation  
44 entering the Earth's atmosphere. Aerosols directly influence the Earth's energy budget and act as  
45 cloud condensation nuclei modifying the cloud structure (e.g., Boucher et al., 2013). Aerosols can  
46 either be produced by ejection into the atmosphere or by physical and chemical processes within the  
47 atmosphere. Aerosol particles affect the radiative field by attenuating the direct component thereby  
48 enhancing (or reducing under a highly absorbing aerosol) the diffuse component. They also produce  
49 indirect effects by perturbing the Earth's atmospheric radiative balance by modulating cloud albedo  
50 and fraction.

51 The aerosol radiative effect (ARE) is defined as the change in net radiation due to changes in  
52 atmospheric aerosol properties and content. This is a key quantity in the determination of climate  
53 change (e.g., Hansen et al., 1998). Most studies dealing with ARE have focused on discrete  
54 wavelengths, whole shortwave (SW) solar radiation spectrum (e.g., Rajeev and Ramanathan, 2001;  
55 García et al., 2008; di Sarra et al., 2008; Foyo-Moreno et al., 2014; Mateos et al., 2013a), longwave  
56 (LW) radiation (e.g., Panicker et al., 2008; di Sarra et al., 2011; Antón et al., 2014), ultraviolet (UV)  
57 interval (e.g., Hatzianastassiou et al., 2004; Kazadzis et al., 2009; Nikitidou et al., 2013), and visible  
58 (VIS) range (e.g., Jayaraman et al., 1998; Horvath et al., 2002; Bush and Valero, 2003; Meloni et  
59 al., 2003). With regards to surface SW radiative effect ( $ARE_{SW}$ ), Di Biagio et al. (2010) obtained  
60 the maximum radiative daily effects for different aerosol types in the central Mediterranean in the  
61 period 2004-2007:  $-61 \text{ Wm}^{-2}$  (desert dust aerosols),  $-26 \text{ Wm}^{-2}$  (urban/industrial - biomass burning  
62 aerosols) and  $-43 \text{ Wm}^{-2}$  (mixed aerosols). All these negative figures point out a cooling of the  
63 Earth's surface. Aerosol radiative effects in the LW range ( $ARE_{LW}$ ) for dust particles are expected  
64 to be smaller than in the SW and with positive sign (see, e.g., di Sarra et al., 2011; Antón et al.,  
65 2014). Hence, this heating effect at the surface can partly offset the cooling induced in the SW

66 range. With respect to the ARE for the UV range ( $ARE_{UV}$ ), Nikitidou et al. (2013) analyzed the  
67 ARE in two different spectral regions in the UV range, 300-315 and 315-360 nm. They found a  
68 stronger attenuation in the UV-B than in the UV-A.

69 The main goal of this study is to evaluate the ARE at the surface over the Iberian Peninsula, which  
70 is a region of great interest because of its geographical position in Southwestern Europe, near the  
71 African continent and the interface between the Atlantic Ocean and the Mediterranean Basin. Thus,  
72 it is affected by frequent desert dust intrusions which modulate the aerosol climatology of the  
73 Iberian Peninsula (Toledano et al., 2007a, Bennouna et al., 2011; Pey et al., 2013; Valenzuela et al.,  
74 2012). In addition, this area is also affected by a great variety of air masses loaded with different  
75 aerosol types: clean continental, polluted plumes of central Europe, and marine aerosols. Hence,  
76 aerosol climatology at six stations (Palencia, Barcelona, Cabo da Roca, Évora, Granada, and El  
77 Arenosillo) is also carried out for different time periods between 2001 and 2012. Aerosol radiative  
78 effects as well as their efficiency are calculated in four regions of the solar spectrum (ultraviolet,  
79 visible, near-infrared, and shortwave) and the relative contribution of each range with respect to the  
80 whole solar spectrum is analyzed as a function of the aerosol properties. Therefore, this study is  
81 intended to contribute to the understanding of the aerosol impact on the radiative budget over the  
82 Iberian Peninsula.

83 This article presents the following outline: detailed descriptions of the aerosol stations and the  
84 database used are performed in Section 2; Section 3 includes the methodology; the results obtained  
85 in the different analyses about the climatology of aerosol properties, aerosol radiative effects, and  
86 aerosol forcing efficiencies are shown and discussed in Sections 4,5, and 6, respectively. Finally,  
87 the main conclusions of this article are summarized in Section 7.

88

89

90 **2. Columnar aerosol optical data**

91 The aerosol data are obtained from the Aerosol Robotic Network (AERONET) (Holben et al.,  
92 1998). Six AERONET sites operating in the Iberian Peninsula are selected in this study: Palencia,  
93 Barcelona, Évora, Cabo da Roca, Granada and El Arenosillo (see Table 1), all of them with a  
94 minimum of 8 years of data sets of continuous observations. These sites present the largest records  
95 of aerosol properties in the Iberian Peninsula in the AERONET network.

96 The standard instrument used in AERONET is the Cimel CE-318 radiometer. It performs direct sun  
97 measurements at several wavelengths in the spectral range 340-1020 nm. Furthermore, the  
98 instrument also measures sky radiance in the solar almucantar and principal plane configurations at  
99 440, 670, 870 and 1020 nm wavelengths. A detailed description of this instrument is provided by  
100 Holben et al. (1998). The direct sun observations are used to derive the spectral aerosol optical  
101 depth (AOD) and the corresponding Ångström exponent. The sky radiances together with the AOD  
102 are employed to retrieve a set of aerosol optical and microphysical properties via inversion methods  
103 (Dubovik and King, 2000; Dubovik et al., 2006). These include particle size distribution, complex  
104 refractive index, single scattering albedo (SSA), phase function, asymmetry parameter, fraction of  
105 non-spherical particles, etc. (see  
106 [http://aeronet.gsfc.nasa.gov/new\\_web/Documents/Inversion\\_products\\_V2.pdf](http://aeronet.gsfc.nasa.gov/new_web/Documents/Inversion_products_V2.pdf)). Data are provided  
107 in three database levels: 1.0 (raw data), 1.5 (cloud-screened) and 2.0 (cloud-screened and quality  
108 assured).

109 The calibration of these instruments is performed following AERONET protocols by the  
110 AERONET-NASA, PHOTONS and RIMA networks approximately every 12 months of operation.  
111 The estimated uncertainty is 0.01-0.02 for AOD (larger at shorter wavelengths) and ~5% for the sky  
112 radiances (Holben et al., 1998). The SSA has an absolute uncertainty of 0.03-0.07 depending on the  
113 aerosol load and type (Dubovik et al., 2000).

114 Level 2.0 aerosol optical depth data have been used in this work. However, it is well-known that  
115 when level 2.0 inversion data are used, the number of available observations of single scattering  
116 albedo (SSA) and asymmetry factor (g) is quite limited because these variables are only considered  
117 reliable when  $\text{AOD}_{440\text{nm}} > 0.4$ <sup>1</sup>. Such AOD is mainly reached in the study region during Saharan  
118 dust or biomass burning events, therefore we would not have information on SSA and g for other  
119 conditions. To solve this issue, we have reduced the threshold of the level 2.0 inversion products.  
120 For this, we started with the level 1.5 data (for those quality-assured almucantar data that reached  
121 level 2.0) and applied the same criteria used by AERONET to produce the level 2.0 regarding the  
122 number of symmetrical angles, retrieval error and solar zenith angle (see  
123 [http://aeronet.gsfc.nasa.gov/new\\_web/Documents/AERONETcriteria\\_final1\\_excerpt.pdf](http://aeronet.gsfc.nasa.gov/new_web/Documents/AERONETcriteria_final1_excerpt.pdf)).

124 However, a less restrictive threshold is applied to the AOD, which we restricted to cases with  
125  $\text{AOD}_{440\text{nm}} > 0.15$ , instead of 0.4. This choice must be considered a compromise between the amount  
126 and the quality of the data. This kind of approach has been adopted by other authors using  
127 AERONET absorption data (e.g., Mallet et al., 2013). The threshold of 0.15 seems adequate for  
128 analyzing the typical values of the AOD in the Iberian Peninsula (e.g., Bennouna et al., 2011;  
129 Obregón et al., 2012), because it can be considered a value to separate background aerosol  
130 conditions from episodic events with moderate or high aerosol loadings. The level 1.5-filtered data  
131 of SSA and g are daily averaged in order to have one value per day. In these conditions, the  
132 estimated uncertainty of the single scattering albedo is  $\pm 0.05\text{--}0.07$  (Dubovik et al., 2000).  
133 Furthermore, for those days presenting level 2.0 data but also measurements in the 1.5-filtered level,  
134 we tested the uncertainty of our approach. We evaluated the difference in the SSA values of the  
135 level 1.5-filtered data with respect to the closest level 2.0 data. The mean relative differences in the

---

<sup>1</sup> Other inversion products, like the volume size distributions, are provided for all AOD levels.

136 SSA values between both methodologies are smaller than 1%, being in the same order of the  
137 inversion uncertainty.

138 Lastly, when the AOD is low (<0.15 at 440 nm), there is no reliable information on the absorption  
139 properties in the almucantar retrievals. Such low AOD is typical in our study region (e.g., almost  
140 70% of observations at Palencia, Granada and Évora are below this threshold). If only cases with  
141  $AOD_{440nm} > 0.15$  are considered in our study, the derived aerosol radiative effect is unrealistically  
142 large. To overcome this problem of representativeness, fixed values of SSA (0.90) and  $g$  (0.75)  
143 have been used for the cases with  $AOD < 0.15$  at 440 nm, considering typical values for  
144 continental, desert, and maritime aerosols (e.g., Hess et al., 1998). In spite of the associated  
145 uncertainties, our approximation (daily level 1.5-filtered values of these aerosol properties for  $AOD$   
146  $> 0.15$  together with a typical fixed value for low  $AOD$  cases) provides a good characterization of  
147 the aerosol absorption of the particles present in the atmosphere. The data products and AERONET  
148 database level are summarized in Table 2, where the estimated absolute uncertainties of  $AOD$  and  
149 SSA are also provided.

150

### 151 **3. Methodology**

152 The ARE calculations are performed in the ultraviolet ( $ARE_{UV}$ , 280-400 nm), visible ( $ARE_{VIS}$ , 400-  
153 700 nm), near-infrared ( $ARE_{NIR}$ , 700-2800 nm), and shortwave ( $ARE_{SW}$ , 280-2800 nm) intervals.  
154 For this purpose, cloud-free simulations are carried out by means of a radiative transfer code.

155 The libRadtran model (Mayer and Kylling, 2005) has been shown to be a useful tool for obtaining  
156 solar radiation data, presenting high accuracy (e.g., Román et al., 2014). Version 1.7 of the  
157 libRadtran is used in this study with inputs of aerosol, total ozone column (TOC), precipitable water  
158 vapor column (PWC), and surface albedo data. We performed simulations of ultraviolet (280-400

159 nm), visible (400-700 nm), near-infrared (700-2800 nm), and shortwave (280-2800 nm) radiation  
160 during the periods indicated in Table 1. Total ozone column is provided by the Ozone Monitoring  
161 Instrument (OMI) and Total Ozone Mapping Spectrometer (TOMS). Daily values of these  
162 instruments are obtained from the Daily Level 3 Global Gridded products, which are downloaded  
163 using the Giovanni application (<http://disc.sci.gsfc.nasa.gov/giovanni>). Level 2.0 AERONET PWC  
164 data are used in the calculations. The uncertainty of this parameter is 10-15% (Holben et al., 1998).  
165 In addition, retrievals of surface albedo at 440, 675, 870 and 1020 nm from the AERONET  
166 algorithm are also used in this work. For land surface cover, this algorithm relies on the Lie–Ross  
167 model (Lucht and Roujean, 2000), but considering the bidirectional reflectance distributions from  
168 MODIS (Moody et al., 2005).

169 Aerosol properties obtained from AERONET measurements are also used as input to the libRadtran  
170 model. Ångström coefficients,  $\alpha$  and  $\beta$ , are utilized to compute a spectral aerosol optical depth in  
171 the wavelengths of interest (Schuster et al., 2006). Ångström exponent  $\alpha$  is obtained with the  
172 measurements between 440 and 870 nm, while the turbidity  $\beta$  is obtained from the  $\alpha$  value and  
173 aerosol data at 1020 nm. Since the aerosol asymmetry factor, single scattering albedo, and surface  
174 albedo are obtained at four wavelengths from AERONET in each measurement, three different  
175 spectral regions are simulated with the libRadtran model. For computations in the UV range (280-  
176 400 nm), the AERONET retrievals of aerosol asymmetry factor, aerosol single scattering albedo,  
177 and surface albedo at 440 nm are used. The AERONET retrievals at 675 nm of the same variables  
178 are used in the visible range (400-700 nm), while in the near-infrared region (700-2800 nm) we  
179 used the average properties retrieved at 870 and 1020 nm. In each interval, these properties are  
180 considered as wavelength independent. This choice to perform the radiative transfer simulations is  
181 proven as adequate in the Appendix A. Other options in the model set-up are: extraterrestrial  
182 irradiance values are taken from Gueymard (2004); profiles of temperature, air density, ozone and  
183 other atmospheric gases are taken from the midlatitude summer/winter standard atmospheres; and

184 the radiative equation solver is the improved version of the discrete ordinate method of Stamnes et  
185 al. (2000) (DISORT2) calculated by 16-streams (e.g., de Miguel et al., 2011). After computing the  
186 solar irradiance in the different spectral intervals, the SW irradiance is evaluated by adding up the  
187 contributions of these three spectral regions.

188 In order to evaluate the aerosol radiative effect, the simulations under aerosol-free conditions are  
189 also computed with the same inputs as explained above, but with a fixed  $\beta$  value of 0.001.

190 The use of radiative transfer models fed with reliable experimental aerosol data to determine the  
191 ARE has been also employed in other studies (e.g., Barja and Antuña, 2011; Valenzuela et al., 2012;  
192 García et al., 2014).

193 Once the simulated radiometric values are obtained, ARE is derived for each interval (X represents  
194 UV, VIS, NIR, and SW) at the surface by:

195

$$196 \text{ARE}_X = (X_{\text{aer}}^{\downarrow} - X_{\text{aer}}^{\uparrow}) - (X_{\text{NOaer}}^{\downarrow} - X_{\text{NOaer}}^{\uparrow}) \quad (1)$$

197

198 where  $X_{\text{aer}}$  and  $X_{\text{NOaer}}$  are the irradiances ( $\text{W m}^{-2}$ ) for the X range under actual and aerosol-free  
199 conditions, respectively.

200 Daily values are obtained by the integration of the hourly data during the whole day (24 h)  
201 considering  $\text{ARE} = 0 \text{ W m}^{-2}$  for  $\text{SZA} > 90^\circ$  (e.g., Bush and Valero, 2003; Valenzuela et al., 2012)  
202 and assuming cloud-free conditions along the day:

203

$$\text{ARE}_{\text{daily}} = \sum \text{ARE}_{\text{hourly}} \frac{dt}{24} \quad (2)$$

204

205 The aerosol forcing efficiency (AFE) is defined as the rate at which the radiative effect varies per  
206 unit of AOD (e.g., Di Biagio et al., 2009; and the references therein). The linear relationship  
207 between aerosol radiative effect and AOD is well known (see, e.g., Costa et al., 2004, 2006; Di  
208 Biagio et al., 2009). Hence, in this study, ARE is obtained as the slope of linear fits in the ARE vs  
209 AOD<sub>500nm</sub> relationships. Therefore, AFE values are expressed in W m<sup>-2</sup> per AOD<sub>500nm</sub>-unit (Wm<sup>-2</sup>τ<sup>-1</sup>).  
210

211 With respect to the temporal trends calculated in this study, the Sen method (Sen, 1968) is applied  
212 to evaluate the slope of a time series using the Mann-Kendall non parametric test to determine the  
213 significance of these rates. The Sen method is not greatly affected by outliers and can be computed  
214 when there are gaps in the database (Collaud Coen et al., 2013). This is a common and adequate  
215 method in temporal trend evaluation (e.g., Sánchez-Lorenzo et al., 2013). The trends calculated in  
216 this study are obtained in the corresponding physical units per year. However, to unify notation with  
217 previous studies dealing with the radiative effect trends of clouds and aerosols (e.g., Mateos et al.,  
218 2013b), the results are multiplied by 10 and expressed in physical units per decade. In this way, the  
219 rates are also easier to read.

220

#### 221 **4. Analysis of aerosol properties over the Iberian Peninsula**

222 A direct CIMEL retrieval (AOD at 440 nm) is selected to perform the climatological analysis  
223 because the estimations of AOD<sub>500nm</sub> (used in the ARE calculations) are obtained using  $\alpha$  values.  
224 Hence, we minimized the impact of other uncertainty sources in the AOD analysis. Besides, the  
225 results for AOD<sub>440nm</sub> and AOD<sub>500nm</sub> do not differ excessively. In order to identify the differences in  
226 the aerosol climatology over the six sites analyzed in this study, the monthly distribution of the

227 daily values of the  $\text{AOD}_{440\text{nm}}$  and  $\alpha$  are evaluated using the database mentioned in Table 1. All the  
228 available level 2.0 AERONET measurements are used in this section.

229 Figure 1 shows the climatology of the aerosol load by box whisker plots. Several conclusions can  
230 be drawn from this figure. The highest values of the AOD occur in Barcelona, as can be expected  
231 because it is a large city. With respect to the monthly average values (triangles in the figure), the  
232 central stations in the Iberian Peninsula (Palencia and Évora) exhibit  $\text{AOD}_{440\text{nm}}$  below 0.2, while the  
233 southern sites (Cabo da Roca, Granada, and El Arenosillo) show aerosol load over 0.2 during  
234 summer months. The  $\text{AOD}_{440\text{nm}}$  seasonal distribution is seen, with maximum values in summer and  
235 minimum ones in winter. However, the seasonality becomes more evident in the stations outside the  
236 central area of the Iberian Peninsula. The large differences between median and average values for  
237 some months evidence a large impact of high aerosol optical depth events on the monthly  
238 climatology. In this line, the bimodality of the monthly AOD climatology (with two maximum  
239 monthly means occurring in March and summer months) observed for the El Arenosillo site has  
240 been already reported by previous studies (e.g., Bennouna et al., 2011), and directly attributed to  
241 desert dust intrusions from the African continent.

242 To go further in the characterization,  $\alpha$  allows for a better understanding of the particle size over  
243 each site. Figure 2 shows the climatology of this variable over the six stations using also box  
244 whisker plots. Analyzing the monthly average means,  $\alpha$  values larger than one, indicative of the  
245 predominance of fine particles, are dominant over Barcelona, Palencia, and Évora. The other three  
246 stations (Cabo da Roca, Granada, and El Arenosillo) present monthly  $\alpha$  averages over and below 1,  
247 which means a larger variety of aerosol sizes over these stations. A seasonal dependence over  
248 Granada site is seen, with winter months dominated by fine particles and summer months by larger  
249 ones (see also Navas-Guzman et al., 2013). Values of  $\alpha$  present a large variability during summer  
250 which is indicative of the influence of different aerosol types including biomass burning events and

251 Saharan dust transport (e.g., Pérez-Ramírez, 2008). The monthly distribution of  $\alpha$  is symmetric with  
252 similar average and median values through the year for the six sites.

253 With the daily AOD and  $\alpha$  values, it is possible to classify the origin of the aerosol particles.  
254 Previous studies suggest different thresholds of AOD and  $\alpha$  (e.g., Hess et al., 1998; Pace et al.,  
255 2006; Toledano et al., 2007b). A simple classification, which can be used for the whole Iberian  
256 Peninsula, of aerosol type is carried out in this study. The threshold between fine and large particles  
257 is placed at  $\alpha = 1$ , while the situations with a high aerosol load are those with  $\text{AOD}_{440\text{nm}} > 0.2$ .  
258 Therefore, aerosol particles can be classified in four types: maritime ( $\text{AOD}_{440\text{nm}} < 0.2$  and  $\alpha < 1$ ),  
259 desert dust ( $\text{AOD}_{440\text{nm}} > 0.2$  and  $\alpha < 1$ ), continental clean ( $\text{AOD}_{440\text{nm}} < 0.2$  and  $\alpha > 1$ ), and  
260 continental polluted ( $\text{AOD}_{440\text{nm}} > 0.2$  and  $\alpha > 1$ ). Note that the limit of  $\text{AOD}_{440\text{nm}} < 0.2$  is arbitrary  
261 and this value could be adjusted according to the sites, which likely produce a different distribution  
262 in the pie diagrams. Even close stations can present slight differences in the  $\alpha$ -AOD classification  
263 (see, e.g., Obregón et al. 2012). However it is not the aim of this work to provide an extensive  
264 aerosol climatology, but rather to demonstrate the great variety of air masses over Iberia which  
265 transport different aerosol types. Although other types, such as biomass burning or mixed aerosols,  
266 are placed in the boundaries of these types, this simple classification can provide information about  
267 the aerosol sources for the six sites. The classification used here is in line with the previous studies.  
268 For instance, Toledano et al., (2007b) proposed for El Arenosillo site similar thresholds (see their  
269 Table V), although they identified continental polluted aerosols with an  $\text{AOD}_{440\text{nm}}$  larger than 0.35  
270 and  $\alpha > 1.4$ . Pace et al., (2006) proposed at Lampedusa island (Central Mediterranean) a desert dust  
271 identification when  $\text{AOD}_{440\text{nm}} \geq 0.15$  and  $\alpha \leq 0.5$ .

272 Figure 3 shows pie diagrams with the frequency of occurrence of the four aerosol types. The six  
273 diagrams agree pointing at continental clean as the main type of aerosols over the Iberian Peninsula.  
274 In Barcelona, there is also an important contribution of continental polluted, since Barcelona is a

275 large coastal city with relevant pollution levels from vehicular and ship traffic (e.g., Reche et al.,  
276 2011). The influence of maritime aerosols is notable at El Arenosillo, Cabo da Roca, and Évora  
277 sites (see also e.g., Bennouna et al., 2011; Obregón et al., 2012). Furthermore, desert dust events are  
278 shown to be common in the Iberian Peninsula with a higher occurrence at Granada and El  
279 Arenosillo sites (the two closest points to the African continent and hence to the Saharan desert)  
280 (see also Toledano et al., 2007b; Guerrero-Rascado et al., 2009; Antón et al., 2012). For instance,  
281 the minimum values of  $\alpha$  obtained for Granada station during summer months are linked to the  
282 higher likelihood of desert dust events (Valenzuela et al., 2012), being sometimes associated with  
283 high aerosol loads (Córdoba-Jabonero et al., 2011). These results corroborate the findings obtained  
284 by previous studies about desert dust events over the Iberian Peninsula (see, e.g., Lyamani et al.,  
285 2005; Toledano et al., 2007b; Cachorro et al., 2008).

286 The inter-annual change of aerosol load can be established over the last decade in the Iberian  
287 Peninsula. The yearly values of  $\text{AOD}_{440\text{nm}}$  at the six sites are shown in Figure 4. The geographical  
288 distribution of AOD through the Spanish geography is observed in the figure. Barcelona site  
289 presents yearly values over ~0.2. Granada, El Arenosillo, and Cabo da Roca exhibit yearly means in  
290 the interval between 0.15 and 0.22, while the means for Palencia and Évora sites are slightly lower  
291 in the range 0.12-0.18. Analyzing the six sites together, the year of 2010 presents one of the  
292 minimum values of  $\text{AOD}_{440\text{nm}}$ , while the maximum averages seem to appear at the early 2000s. The  
293 different sampling of AOD measurements in the six sites can produce discrepancies because  
294 different events are or are not captured in each database. In addition, possible technical problems  
295 and meteorological conditions (CIMEL aerosol data are recorded under cloud-free skies) cause a  
296 non-equally distribution through the year. Overall, summer is the season with the largest  
297 contribution of data, followed by spring, autumn, and winter. Looking at the years with a large  
298 sampling (>200 days in, at least, four stations), 2005, 2007, and 2011, all the features mentioned  
299 above are corroborated for these particular years. The minimum of 2010 occurs when two Southern

300 sites (El Arenosillo and Cabo da Roca) have not enough data to evaluate the yearly mean. Hence,  
301 we cannot ensure that the apparent minimum of AOD recorded that year is linked to global-scale  
302 phenomena or to more local conditions at the other sites. During 2010 a persistent negative phases  
303 of North Atlantic Oscillation (NAO) and Quasi Biennal Oscillation (QBO) indices was observed  
304 (e.g., Steinbrecht et al., 2011), and the connection between air mass transport at global scale and  
305 particulate matter (at the surface) is proved by Pey et al., (2013) in the Eastern Iberian Peninsula.

306 With respect to the temporal change, the evolution of these yearly values seems to be weak, which  
307 can be attributed to the large variability observed in the mean values, affected by different  
308 conditions and phenomena. In spite of this, the evaluation of the trend rates (see Section 3 for  
309 details) produces the more statistically significant change for the Barcelona site, where a decrease  
310 of the aerosol load of 0.09 AOD<sub>440nm</sub>-unit per decade is observed with a *p value* of 0.02. The  
311 AOD<sub>440nm</sub> temporal change for the other sites exhibits *p values* over 0.05. Hence, non-statistically  
312 significant results are obtained for the other sites. In spite of that, the sign of all temporal rates is  
313 negative. Hence, a slight reduction of the aerosol load over the Iberian Peninsula can be deduced  
314 since 2000 from the annual values. This result obtained in the Southeastern Europe is in line with  
315 the long-term analysis of AOD series performed in Northern Germany and Switzerland by  
316 Ruckstuhl et al. (2008). These authors highlight a strong decrease of aerosol load starting in 1985,  
317 while the values are stabilized since about 2000.

318 The reasons behind the decrease in the aerosol load since the early 2000s are a mix of  
319 anthropogenic and natural sources. As was reported by Aas et al. (2013), the particulate matter  
320 (PM) emissions in the Iberian Peninsula have decreased around 25% between 2000 and 2011.  
321 Furthermore, observational PM data in different Spanish sites have also shown a decrease trend in  
322 the 2000s (e.g., Barmpadimos et al., 2012; Cusack et al., 2012; Pey et al., 2013; Bennouna et al.,  
323 2014; Mateos et al., 2014). This fact can be understood by the effect of the current economic crisis

324 and the implementation of new environmental laws to control the pollution (e.g., Querol et al.,  
325 2014). In addition, recent studies have shown that natural aerosols have also decreased in the last  
326 decade. For instance, Gkikas et al. (2013) reported, using satellite AOD estimations, that strong and  
327 extreme desert dust episodes in the Mediterranean decreased in the period 2000-2007 over land  
328 surfaces. This change is understood due to the low spring and summer frequencies in 2005 and  
329 2007 and the high frequencies in 2000 and 2003. As it was shown by Pey et al. (2013), one possible  
330 reason behind this change is the atypical trajectories followed by the air masses emerging from  
331 North Africa in summer since 2006. Hence, both columnar and surface aerosols have pointed out a  
332 decrease in the aerosol load over the Iberian Peninsula, which has increased solar radiation levels  
333 reaching the surface in the 2000s (Mateos et al., 2014).

334

### 335 **5. Inter-annual and intra-annual evolution of ARE**

336 From the daily data, the yearly ARE for each station and spectral range is evaluated to analyze the  
337 inter-annual changes (see Figure 5). In spite of the high variability of the yearly values with large  
338 standard deviations (see the vertical bars for Palencia station in the figure), the radiative effects of  
339 atmospheric aerosols have slightly declined over the last years. The patterns of ARE in the UV,  
340 VIS, NIR, and SW ranges are similar, since the inter-annual changes are simultaneously observed in  
341 the four spectral intervals. With respect to the geographical distribution, Barcelona and Granada  
342 sites exhibit the largest effects (more negative ARE), which is in line with the large values of  
343 AOD<sub>440nm</sub> shown in Figure 4. The weakest aerosol effect (less negative ARE) is observed in  
344 Palencia and Évora sites, which is again linked to the lower yearly AOD<sub>440nm</sub>.

345 To establish the general behavior of the ARE over the whole Iberian Peninsula, the yearly values  
346 using the six ground-based stations are evaluated. Only those years with, at least, simultaneous  
347 measurements at three sites are considered in these averages, and consequently, the time period is

348 limited to 2004-2012. Figure 6 shows the evolution of the ARE and AOD at 500 nm for the entire  
349 peninsula. The decline of the AOD for this mean series produces a consequent decrease in the  
350 aerosol radiative effect at the four spectral ranges. The temporal trends of these yearly values are  
351 evaluated, and all the trends shown in Figure 6 resulted with *p values* between 0.004 and 0.03.  
352 Overall,  $ARE_{SW}$  over the Iberian Peninsula increased  $3.6 \text{ W m}^{-2}$  per decade (*p value* = 0.028) while  
353 the aerosol reduced  $0.04 \text{ AOD}_{500\text{nm}}$ -unit per decade (*p value* = 0.006). Furthermore, this reduction in  
354 the radiative effects of the atmospheric aerosol over the Iberian Peninsula could partially contribute  
355 to the increase in the levels of SW radiation at the surface (the brightening phenomenon) in this  
356 region reported by, e.g., Sanchez-Lorenzo et al. (2013) and Mateos et al. (2013b).

357 The yearly aerosol radiative effects over the entire peninsula are in the ranges:  $-1.1 < ARE_{UV} < -0.7 \text{ W m}^{-2}$ ,  
358  $-5.7 < ARE_{VIS} < -3.5 \text{ W m}^{-2}$ ,  $-2.6 < ARE_{NIR} < -1.6 \text{ W m}^{-2}$ , and  $-8.8 < ARE_{SW} < -5.7 \text{ W m}^{-2}$ .  
359 The larger contribution of the visible spectral region with respect to the whole solar spectrum was  
360 also noticed by Bush and Valero (2003), and this is expected since the maximum of shortwave  
361 radiation is found in this interval. The relationship between ARE and  $AOD_{500\text{nm}}$  is analyzed more in  
362 detail in Section 6, when the aerosol forcing efficiency is evaluated for each ground-based station.

363 In addition to the inter-annual changes, the intra-annual behavior is also analyzed. For this purpose,  
364 the annual cycle (12 monthly means) is evaluated for the six stations (see Figure 7). A seasonal  
365 pattern is seen in  $ARE_{UV}$  and  $ARE_{VIS}$ , and therefore,  $ARE_{SW}$ . However,  $ARE_{NIR}$  does not follow a  
366 seasonal pattern, particularly at the Évora and Palencia stations given that  $ARE_{NIR}$  remains nearly  
367 constant. Small differences among the six stations are observed in the annual cycle during the cold  
368 seasons. The aerosol radiative effects are stronger during summer months. This can be related to the  
369 higher likelihood of desert dust or biomass burning events over the Iberian Peninsula in these  
370 months (e.g., Cachorro et al., 2008; Valenzuela et al., 2012), as was mentioned above. This is  
371 corroborated by the increase of the differences among the stations during the warm season, likely

372 due to the variability in the impact of the desert dust episodes which strongly depend on the  
373 geographical location of each site. The higher occurrence of large aerosol loads during the warm  
374 seasons (see Figure 1), can explain the more negative ARE during summer and spring in Figure 7.  
375 For instance, the Barcelona station, with the largest values of  $AOD_{440\text{nm}}$ , is the bottom curve of each  
376 panel in Figure 7. Furthermore, the influence of mineral dust aerosol (with high aerosol optical  
377 depth) during these months also causes strong radiative effects, as was also reported by previous  
378 studies (e.g., Cachorro et al., 2008; Guerrero-Rascado et al., 2009; Antón et al., 2011; Román et al.,  
379 2013; García et al., 2014). In addition, the bimodality of the monthly AOD climatology mentioned  
380 in Section 4 has its impact on the radiative effects. The annual AOD cycle (see Figure 1, El  
381 Arenosillo site) causes the inverse monthly distribution of ARE with a first minimum in March.  
382 This effect is more clearly seen in  $ARE_{\text{NIR}}$  and  $ARE_{\text{SW}}$ .

383

## 384 **6. Aerosol radiative forcing efficiency in different spectral ranges**

385 The daily AFE values are calculated (following the methodology described in Section 3) in all the  
386 spectral ranges. The AFE is a function of the aerosol optical properties, where both the aerosol  
387 particle size distribution and absorptive properties play a key role (e.g., Antón et al., 2011). As we  
388 assumed a fixed value of  $SSA = 0.90$  in the simulations with  $AOD_{440\text{nm}} < 0.15$  (see Table 2), the  
389 AFE is calculated only for those cases showing  $AOD_{440\text{nm}}$  larger than 0.15.

390 To identify the influence of  $SSA$  and  $\alpha$  on AFE, this variable is calculated for several intervals of  
391 each aerosol property. Four categories of single scattering albedo at 675 nm are established in the  
392 calculation of the AFE:  $1.0 \geq SSA_1 > 0.95$ ,  $0.95 \geq SSA_2 > 0.90$ ,  $0.90 \geq SSA_3 > 0.85$ , and  $0.85 \geq$   
393  $SSA_4 > 0.80$ . Furthermore, aerosol size is classified in three intervals:  $0 \leq \alpha_1 \leq 1$ ,  $1 < \alpha_2 \leq 1.5$ , and  
394  $1.5 < \alpha_3 \leq 2$ . Note that two intervals in the range of  $\alpha$  larger than 1 have been considered. One for  
395 median particles and another one for fine particles, because of the relevant importance of median

396 size particle (continental or mixed aerosol aerosols types) over the Iberian Peninsula (see Figure 3).  
397 Although the general classification between fine and coarse particles requires a more refined  
398 classification (Schuster et al., 2006; Prats et al., 2011), the more general intervals selected in this  
399 study are adequate to perform a study of the aerosol sizes at the six stations together.  
  
400 Figure 8 shows the AFE obtained for the UV ( $AFE_{UV}$ ), VIS ( $AFE_{VIS}$ ), NIR ( $AFE_{NIR}$ ), and SW  
401 ( $AFE_{SW}$ ) ranges for all these intervals. The threshold to evaluate the average in each sub-interval is  
402 fixed at 10 data points. From these figures it is seen that, the stronger the absorption by aerosols, the  
403 stronger their forcing efficiency. That is a decrease in the absolute values of the AFE for increasing  
404 SSA and for all particle size. In general, the groups of non-absorbing particles exhibit a good  
405 agreement among the six stations (see, for instance, AFE values in all the spectral ranges in the  
406 interval  $1 < \alpha \leq 1.5$ ). Larger differences are obtained in the case of more absorbing aerosol particles.  
407 These can be understood because of the different types of aerosols presented over each site (see  
408 Section 4) and the different data numbers. The average AFE values over the whole Iberian  
409 Peninsula (considering the six stations together) are presented in Table 3 as a function of  $\alpha$  and  
410 SSA, separately. The role played by the aerosol size on AFE values is different in the three sub-  
411 intervals of the shortwave radiation. The  $AFE_{UV}$  and  $AFE_{VIS}$  are larger (in absolute value) for fine  
412 particles, while the opposite occurs in the case of  $AFE_{NIR}$ . As a result of these mixed effects,  $AFE_{SW}$   
413 shows also a decrease in its values with increasing  $\alpha$ , but this effect is weaker than for the visible  
414 and ultraviolet parts. SSA exhibits a more dominant role. As was observed before, the most  
415 negative values are achieved for the most absorbing aerosols considered in this study (group 1 of  
416 SSA, see Table 3).  
  
417 The average values of forcing efficiency obtained in this study (see Table 3) are in line with those  
418 found by other authors. Table 4 summarizes the results obtained by previous studies. It is difficult to  
419 assess some features in the comparison with previous reported AFE values, because of the different

420 aerosol types, time periods and methods that are analyzed. Our study presents the evaluation of  
421 ARE with six long-term databases of aerosol properties. In spite of that, the values shown in Table  
422 3 agree with those of Table 4, but the larger discrepancies are observed with the studies focusing on  
423 specific events. Our results match better with the results reported by, e.g., Zhou et al. (2005),  
424 Meloni et al. (2005), and Di Biagio et al. (2010). As was noticed by, e.g., Costa et al. (2004, 2006)  
425 and Di Biagio et al. (2010), AFE at the surface is larger (in absolute term) for aerosols characterized  
426 by smaller and absorbing particles. This result is corroborated by the findings shown in this study.  
427 Furthermore, as was pointed out by Di Biagio et al. (2010), the aerosol absorption is the dominant  
428 factor on AFE evaluated at the surface.

429 To evaluate the contribution of each spectral range with respect to the shortwave, the dependence of  
430 each AFE ratio (VIS to SW and NIR to SW) on SSA and  $\alpha$  is shown in Figure 9. The  
431  $AFE_{VIS}/AFE_{SW}$  and  $AFE_{NIR}/AFE_{SW}$  ratios are shown in the figure since their contributions are the  
432 dominant.  $AFE_{UV}/AFE_{SW}$  ratio can be obtained as 100% minus the sum of the percentage of the two  
433 other ranges. As expected, non substantial differences are observed in the behavior of the six  
434 stations considered in this study. The NIR contribution becomes more decisive for large particles ( $\alpha$   
435  $< 1$ ). It is expected that larger particles interact more with the longer wavelengths, while the smaller  
436 particles present more interaction with the shorter wavelengths. The presence of large particles with  
437 low SSA (high absorption) leads to a reduction of the  $AFE_{NIR}/AFE_{SW}$  ratio as well as an increase of  
438 the  $AFE_{VIS}/AFE_{SW}$  ratio. However, for non-absorbing (high SSA) large particles, the  
439  $AFE_{NIR}/AFE_{SW}$  ratio increases, and the contributions of the visible and infrared parts become more  
440 similar (both around ~40-50%). The difference between  $AFE_{VIS}/AFE_{SW}$  and  $AFE_{NIR}/AFE_{SW}$   
441 increases for intermediate - fine particles. For these particles, the  $AFE_{VIS}/AFE_{SW}$  ratio does not  
442 show a dependence on SSA. The smallest contribution of the NIR interval is around ~25% under  
443 strong absorbing aerosols and fine particles, while  $AFE_{VIS}/AFE_{SW}$  is still over 60%. For this case,  
444 the contribution of the ultraviolet range achieves a maximum of ~15%, being almost comparable

445 with the near infrared contribution. In summary, aerosol size determines the relevance of VIS-NIR  
446 ranges, while SSA plays a key role, particularly, for large particles.

447

448 **7. Conclusions**

449 Six long-term datasets of aerosol properties over the Iberian Peninsula were analyzed and used as  
450 input in a radiative transfer model to simulate ultraviolet, visible, near-infrared, and shortwave  
451 radiation. The aerosol radiative effect (ARE) and aerosol forcing efficiency (AFE) were calculated.

452 The main conclusions are as follows:

453 1) The AOD and  $\alpha$  annual cycles over the six analyzed sites present high variability among them,  
454 emphasizing the inhomogeneity of the Iberian Peninsula, mainly due to the different predominant  
455 aerosol types over each station. The Barcelona site presents the largest AOD values, although  
456 Southern locations (Granada and El Arenosillo sites) frequently exhibit daily mean AOD values  
457 exceeding 0.2 during the summer months. The  $\alpha$ -AOD classification scheme has shown that  
458 continental (mainly, clean) is the predominant aerosol type over the Iberian Peninsula. However,  
459 maritime aerosols are also frequent at the Cabo da Roca, El Arenosillo and Évora sites. Desert dust  
460 events are registered at the six sites, with the highest frequency at Granada and El Arenosillo, but  
461 the most relevant feature is the South-North (decreasing) gradient of desert dust load which  
462 modulates the aerosol climatology over the Iberian Peninsula.

463 2) In the whole Iberian Peninsula, yearly  $ARE_{UV}$  ranges between  $-1.1$  and  $-0.7 \text{ Wm}^{-2}$ ,  $ARE_{VIS}$   
464 ranges between  $-5.7$  and  $-3.6 \text{ Wm}^{-2}$ , and  $ARE_{NIR}$  has values between  $-2.6$  and  $-1.6 \text{ Wm}^{-2}$ . As a  
465 result,  $ARE_{SW}$  is in the range between  $-8.8$  and  $-5.7 \text{ Wm}^{-2}$ . The temporal changes of  $ARE_{UV}$ ,  
466  $ARE_{VIS}$ ,  $ARE_{NIR}$ , and  $ARE_{SW}$  exhibit positive statistically significant trends between 2004 and  
467 2012. For instance, the change rate for the  $ARE_{SW}$  is  $+3.6 \text{ Wm}^{-2}$  per decade (statistically significant

468 at the 95% confidence level). This decrease in the aerosol radiative effects (since ARE values are  
469 negative) is in line with a slight AOD decrease over in the Iberian Peninsula in the last decade.

470 3) The intra-annual ARE cycle exhibits larger values during spring and summer, when the  
471 occurrence of high aerosol loading episodes over the Iberian Peninsula is more frequent. In general,  
472 the annual AOD cycle is driven by the occurrence of Saharan dust events.

473 4) The AFE values at the six sites used in this study are in good agreement. Conditions of high  $\alpha$   
474 (small particle predominance) and low SSA (high absorption) lead to the largest negative AFE  
475 values. Overall, as an average for the Iberian Peninsula:  $AFE_{UV} = -6 \text{ Wm}^{-2}\tau^{-1}$ ,  $AFE_{VIS} = -34 \text{ Wm}^{-2}\tau^{-1}$ ,  
476  $AFE_{NIR} = -19 \text{ Wm}^{-2}\tau^{-1}$ , and  $AFE_{SW} = -59 \text{ Wm}^{-2}\tau^{-1}$ .

477 5) The contribution of the ultraviolet, visible, and infrared spectral ranges to total shortwave aerosol  
478 forcing efficiency is governed by the aerosol type. In general, the visible part of the spectrum is the  
479 most dominant part. Non-absorbing large particles cause more even contribution of VIS and NIR  
480 intervals to the AFE, while the UV range shows a higher contribution in case of absorbing fine  
481 particles.

482

483

#### 484 **Appendix A**

485 The two choices in the performance of radiative transfer simulations from the libRadtran code  
486 concerning aerosol properties are justified in this section.

487 First at all, as it is mentioned in the text, most of the data present  $AOD_{440\text{nm}} < 0.15$  (~70% for  
488 Palencia, Granada, and Évora sites). For these low values,  $SSA = 0.9$  and  $g = 0.75$  are selected by  
489 the representativeness of the local aerosols in the six sites of study (e.g., Cachorro et al., 2010). To

490 analyze possible uncertainties emerging from this choice, the radiative net fluxes are also evaluated  
491 for SSA and  $g$  values covering the most variety of aerosols observed in the Iberian Peninsula.  
492 Hence,  $SSA_1 = 0.8$ ,  $SSA_2 = 1.0$ ,  $g_1 = 0.65$ , and  $g_2 = 0.80$  are selected in this analysis. Four  
493 possibilities or scenarios are simulated mixing the two values of the aerosol properties. The  
494 radiation obtained in each scenario is compared with the assumed case of  $SSA = 0.9$  and  $g = 0.75$ .  
495 The two optical properties are also fixed as non-wavelength-dependent in this analysis. The  
496  $AOD_{440nm}$  used is 0.15, the worst scenario possible for these cases because the higher the AOD the  
497 stronger the impact of aerosol properties. The simulations are performed for the four spectral  
498 ranges. Table A1 shows the mean relative difference observed for the four scenarios and two  
499 different SZAs ( $30^\circ$  and  $60^\circ$ ). The assumption considered in this study causes, in the worst possible  
500 scenarios, errors in the ARE retrievals (obtained as the expanded errors from the radiative  
501 uncertainty)  $< 10\%$ ,  $< 6\%$ ,  $< 3\%$ , and  $< 5\%$  for the UV, VIS, NIR, and SW ranges, respectively. As  
502 the cases with  $AOD_{440nm} < 0.15$  are the large majority of the Iberian Peninsula, they should be  
503 included in the study. The experimental retrievals of SSA and  $g$  for these cases with low AOD  
504 present large uncertainties, and no reliable information can be used to verify our assumption.  
505 Hence, the results of this sensitivity study are adequate. As the SSA influences the diffuse radiation,  
506 the worst results are obtained at large SZAs. The impact of  $g$  on the net fluxes is very weak. In  
507 conclusion, the choice of  $SSA = 0.9$  and  $g = 0.75$  in a clean scenario ( $AOD_{440nm} < 0.15$ ) is proven as  
508 adequate because of two reasons: a) representativeness of the local aerosols which can be mixture  
509 of different types, and b) the low uncertainty produced in the simulations by SSA and  $g$  under these  
510 conditions.

511 The choice of fixed SSA and  $g$  values within each of the spectral ranges (UV, VIS, and NIR)  
512 represented by the CIMEL spectral measurements is also justified here. The aerosol models by  
513 Shettle (1989) included in the libRadtran code (see Mayer and Kylling, 2005) are used to evaluate  
514 the uncertainty of using this approximation. The continental clean aerosols (most common type in

515 the Iberian Peninsula, see Figure 3), and continental polluted aerosols (also very common, which  
516 present an extreme case of absorption) are tested in this analysis. The simulations are performed for  
517 the expected spectral behavior of SSA and  $g$  following Shettle (1989) and the case of fixed  
518 properties in the UV (SSA and  $g$  values at 440 nm), VIS (SSA and  $g$  values at 675 nm), and NIR  
519 intervals (SSA and  $g$  average of values at 870 and 1020 nm). Figure A1 presents the evolution of  
520 the relative error (considering as reference the net flux with the expected spectral dependence of  
521 aerosol properties) for several AOD values between aerosol-free and  $AOD_{550\text{nm}} = 0.6$ . In the case of  
522 continental clean aerosols (Figure A1.a), the error of using our assumption is lower than 5% for all  
523 SZAs and spectral ranges. Therefore, as the large majority of aerosol particles are of this type, the  
524 methodology used and proposed in this study only introduces a relative error below 5% in the  
525 majority of the simulations. With respect to the continental polluted aerosols (Figure A1.b), the  
526 error increases achieving a maximum around 20% for the UV range and very turbid conditions. For  
527 large AOD conditions in the Iberian Peninsula (e.g.,  $AOD_{550\text{nm}} = 0.4$ ) but with low frequency of  
528 occurrence in contrast to  $AOD_{440\text{nm}} < 0.15$ , the error of the SW range is below 5%. However, the  
529 UV range is more sensitive to our method and the error is around 15% at  $SZA = 60^\circ$ . As it was  
530 mentioned above, the errors are larger for large SZAs because of the possible interaction between  
531 absorption and scattering processes resulting the diffuse radiation. The visible range is more  
532 sensitive to the spectral variations than the NIR interval, which exhibits a maximum error around  
533 11% at  $SZA = 60^\circ$  and  $AOD_{550\text{nm}} = 0.6$ . The daily net radiative fluxes are also evaluated for the two  
534 aerosol types in order to quantify the uncertainty in the final simulated data used in this study. For  
535 Palencia site (and the corresponding SZA evolution), a daily value for the June 20th is simulated  
536 assuming  $TOC = 300$  DU and  $PWC = 1$  cm. The results for the continental polluted case with  
537  $AOD_{440\text{nm}} = 0.4$  exhibit differences between the spectral and fixed-band aerosol properties of: 7.5%,  
538 5.3%, 4.0%, and 4.8% for the UV, VIS, NIR, and SW intervals. The relative errors for the same  
539 intervals with continental clean (and same AOD value) are: 1.9%, 1.2%, 1.4%, and 1.4%,

540 respectively. Therefore, the uncertainty due to fixed optical properties in each spectral range is  
541 dependent on the aerosol type but the error caused can be considered as acceptable. Since actual  
542 aerosols often present mixtures of different types, the uncertainty of using the theoretical spectral  
543 evolution for one type (given by an aerosol model) can also produce uncertainties which should be  
544 taken into account. Although other aerosol types are not tested in this analysis, a similar behavior  
545 can be expected. For instance, for the case of desert dust aerosols, Román et al. (2013) found a  
546 slight influence of spectral aerosol absorption properties on UV irradiance analyzing a strong  
547 Saharan intrusion over Granada site.

548 Therefore, the two assumptions performed in this study in the simulations are adequate for the  
549 evaluation of net fluxes and aerosol radiative effects. The uncertainties that can be introduced in the  
550 daily values are acceptable being around or smaller than 5% for the net SW radiation. This  
551 uncertainty is usually achieved in clear-sky modeling (e.g., Mateos et al., 2013a).

552

### 553 **Acknowledgments**

554 The work is supported by the Spanish Ministry of Science and Technology (currently MINECO)  
555 through projects CGL2010-18782, CSD2007-00067, CGL2011-29921-C02-01, CGL2011-23413,  
556 CGL2011-24891, CGL2011-13085-E, CGL2011-13580-E, CGL2012-33576, and CGL2012-  
557 33576; FEDER (Programa Operacional Factores de Competitividade - COMPETE). Also by  
558 Portuguese funding through FCT - Fundação para a Ciência e a Tecnologia in the framework of  
559 project FCOMP-01-0124-FEDER-009303 (PTDC / CTE-ATM / 102142 / 2008); the Évora  
560 Geophysics Centre, Portugal, under the contract with FCT, PEst-OE/CTE/UI0078/2014; and the  
561 Andalusia Regional Government through projects P08- RNM-3568 and P10-RNM-6299. The  
562 research leading to these results has received also funding from the European Union Seventh  
563 Framework Programme (FP7/2007-2013) under grant agreement Nr. 262254 [ACTRIS]. Manuel

564 Antón and Carlos Toledano thank Ministerio de Ciencia e Innovación and Fondo Social Europeo  
565 for the awards of a postdoctoral grant (Ramón y Cajal), and Mar Sorribas for postdoctoral grant  
566 (Juan de la Cierva). We must specially thank the AERONET-GSFC, PHOTONS-LOA and RIMA-  
567 GOA-UVa staff for their scientific and technical support. Ozone Monitoring Instrument (OMI) and  
568 Total Ozone Mapping Spectrometer (TOMS) ozone column data were obtained from the Giovanni  
569 online data system, developed and maintained by the NASA GES DISC.

570

## 571 **References**

572 Aas, W., Espen Yttri, K., Stohl, A., Lund Myhre, C., Karl, M., Tsyro, S., Marečková, K.,  
573 Wankmüller, R., Klimont, Z., Heyes, C., Alastuey, A., Querol, X., Pérez, N., Moreno, T.,  
574 Lucarelli, F., Areskoug, H., Balan, V., Cavalli, F., Putaud, J.P., Cape J.N., Catrambone, M.,  
575 Ceburnis, D., Conil, S., Gevorgyan, L., Jaffrezo, J.L., Hueglin, C., Mihalopoulos, N.,  
576 Mitosinkova, M., Riffault, V., Sellegrí, K., Spindler, G., Schuck, T., Pfeffer, U., Breuer, L.,  
577 Adolfs, D., Chuntonova, L., Arabidze, M., and Abdulazizov, E.: Transboundary particulate  
578 matter in Europe Status report 2013, EMEP Report, 4/2013 (Ref. O-7726), ISSN: 1504-6109  
579 (print), 1504-6192 (online), 2013.

580 Antón, M., Gil, J.E., Fernández-Gálvez, J., Lyamani, H., Valenzuela, A., Foyo-Moreno, I., Olmo, F.  
581 J., and Alados-Arboledas, L.: Evaluation of the aerosol forcing efficiency in the UV erythemal  
582 range at Granada, Spain, *J. Geophys. Res.*, 116, D20214, doi:10.1029/2011JD016112, 2011.

583 Antón, M., Valenzuela, A., Cazorla, A., Gil, J.E., Fernández-Gálvez, J., Lyamani, H., Foyo-  
584 Moreno, I., Olmo, F.J., Alados-Arboledas, L.: Global and diffuse shortwave irradiance during a  
585 strong desert dust episode at Granada (Spain), *Atmos. Res.*, 118, 232–239,  
586 doi:10.1016/j.atmosres.2012.07.007, 2012.

587 Antón, M., Valenzuela, A., Mateos, D., Alados, I., Foyo-Moreno, I., Olmo, F.J., Alados-Arboledas,  
588 L.: Lonwave aerosol radiative effects during an extreme desert dust event in Southeastern  
589 Spain, *Atmos. Res.*, doi: 10.1016/j.atmosres.2014.05.022, 2014.

590 Barja, B., and Antuña, J.C.: The effect of optically thin cirrus clouds on solar radiation in  
591 Camagüey Cuba. *Atmos. Chem. Phys.*, 11, 8625–8634, doi:10.5194/acp-11-8625-2011, 2011.

592 Barmpadimos, I., Keller, J., Oderbolz, D., Hueglin C., and Prèvôt, A.S.H.: One decade of parallel  
593 fine (PM<sub>2.5</sub>) and coarse (PM<sub>10</sub>- PM<sub>2.5</sub>) particulate matter measurements in Europe: trends and  
594 variability, *Atmos. Chem. Phys.* 12, 3189-3203, doi: 10.5194/acp-12.3189-2012, 2012.

595 Bennouna, Y., Cachorro, V., Toledano, C., Berjón, A., Prats, N., Fuertes, D., Gonzalez, R.,  
596 Rodrigo, R., Torres, B., and de Frutos, A.: Comparison of atmospheric aerosol climatologies  
597 over southwestern Spain derived from AERONET and MODIS, *Rem. Sen. Env.* 115, 1272-  
598 1284, 2011.

599 Bennouna, Y.S., Cachorro, V., Burgos, M.A., Toledano, C., Torres, B., and de Frutos, A.:  
600 Relationships between columnar aerosol optical properties and surface Particulate Matter  
601 observations in north-central Spain from long-term records (2003-2011), *Atmos. Meas. Tech.*  
602 *Discuss.*, 7, 5829-5882, doi:10.5194/amtd-7-5829-2014, 2014.

603 Boucher, O., Randall, D., Artaxo, P., Bretherton, C., Feingold, G., Forster, P., Kerminen, V.-M.,  
604 Kondo, Y., Liao, H., Lohmann, U., Rasch, P., Satheesh, S.K., Sherwood, S., Stevens, B., and  
605 Zhang, X.Y.: Clouds and aerosols. In *Climate Change 2013: The Physical Science Basis.*  
606 Contribution of Working Group I to the Fifth Assessment Report of the Intergovernmental  
607 Panel on Climate Change. T.F. Stocker, D. Qin, G.-K. Plattner, M. Tignor, S.K. Allen, J.  
608 Doschung, A. Nauels, Y. Xia, V. Bex, and P.M. Midgley, Eds. Cambridge University Press,  
609 571-657, 2013.

610 Bush, B. C., and Valero, F. P. J.: Surface aerosol radiative forcing at Gosan during the ACE– Asia  
611 campaign, *J. Geophys. Res.*, 108(D23), 8660, doi:10.1029/2002JD003233, 2003.

612 Cachorro, V. E., Toledano, C., Prats, N., Sorribas, M., Mogo, S., Berjón, A., Torres, B., Rodrigo,  
613 R., de la Rosa, J., and De Frutos, A. M.: The strongest desert dust intrusion mixed with smoke  
614 over the Iberian Peninsula registered with Sun photometry, *J. Geophys. Res.*, 113, D14S04,  
615 doi:10.1029/2007JD009582, 2008.

616 Cachorro, V. E., Toledano, C., Antón, M., Berjón, A., de Frutos, A., Vilaplana, J. M., Arola, A., and  
617 Krotkov, N. A.: Comparison of UV irradiances from Aura/Ozone Monitoring Instrument  
618 (OMI) with Brewer measurements at El Arenosillo (Spain) – Part 2: Analysis of site aerosol  
619 influence, *Atmos. Chem. Phys.*, 10, 11867-11880, doi:10.5194/acp-10-11867-2010, 2010.

620 Collaud Coen, M., Andrews, E., Asmi, A., Baltensperger, U., Bukowiecki, N., Day, D., Fiebig, M.,  
621 Fjaeraa, A. M., Flentje, H., Hyvärinen, A., Jefferson, A., Jennings, S. G., Kouvarakis, G.,  
622 Lihavainen, H., Lund Myhre, C., Malm, W. C., Mihopoulos, N., Molenar, J. V., O'Dowd, C.,  
623 Ogren, J. A., Schichtel, B. A., Sheridan, P., Virkkula, A., Weingartner, E., Weller, R., and  
624 Laj, P.: Aerosol decadal trends – Part 1: In-situ optical measurements at GAW and IMPROVE  
625 stations, *Atmos. Chem. Phys.*, 13, 869-894, doi:10.5194/acp-13-869-2013, 2013.

626 Córdoba-Jabonero, C., Sorribas, M., Guerrero-Rascado, J.L., Adame, J.A., Hernández, Y.,  
627 Lyamani, H., Cachorro, V., Gil, M., Alados-Arboledas, L., Cuevas, E., and de la Morena, B.:  
628 Synergetic monitoring of Saharan dust plumes and potential impact on surface: a case study of  
629 dust transport from Canary Islands to Iberian Peninsula, *Atmos. Chem. Phys.*, 11, 3067-3091,  
630 doi:10.5194/acp-11-3067-2011, 2011.

631 Costa, M. J., Levizzani, V., and Silva, A. M.: Aerosol Characterization and Direct Radiative  
632 Forcing Assessment over the Ocean. Part II: Application to Test Cases and Validation. *J. Appl.*  
633 *Meteor.*, 43, 1818–1833, doi: <http://dx.doi.org/10.1175/JAM2157.1>, 2004.

634 Costa, M.J., Sohn, B.J., Levizzani, V., and Silva, A.M.: Radiative forcing of Asian dust determined  
635 from the synergized GOME and GMS satellite data - A case study, *J. Meteorol. Soc. Jpn.*,  
636 84(1), 85-95, doi: [10.2151/jmsj.84.85](https://doi.org/10.2151/jmsj.84.85), 2006.

637 Cusack, M., Alastuey, A., Pérez, N., Pey, J., and Querol, X.: Trends of particulate matter (PM<sub>2.5</sub>)  
638 and chemical composition at a regional site in the Western Mediterranean over the last nine  
639 years (2002-2010), *Atmos. Env.* 12, 8341-8357, doi: [10.5194/acp-12-8341-2012](https://doi.org/10.5194/acp-12-8341-2012), 2012.

640 de Miguel, A., Mateos, D., Bilbao, J., and Román, R.: Sensitivity analysis of ratio between  
641 ultraviolet and total shortwave solar radiation to cloudiness, ozone, aerosols and precipitable  
642 water, *Atmos. Res.*, 102, 136–144, doi:[10.1016/j.atmosres.2011.06.019](https://doi.org/10.1016/j.atmosres.2011.06.019)., 2011.

643 Di Biagio, C., di Sarra, A., Meloni, D., Monteleone, F., Piacentino, S., and Sferlazzo, D.:  
644 Measurements of Mediterranean aerosol radiative forcing and influence of the single scattering  
645 albedo, *J. Geophys. Res.*, 114, D06211, doi:[10.1029/2008JD011037](https://doi.org/10.1029/2008JD011037), 2009.

646 Di Biagio, C., di Sarra, A., and Meloni, D.: Large atmospheric shortwave radiative forcing by  
647 Mediterranean aerosols derived from simultaneous ground-based and spaceborne observations  
648 and dependence on the aerosol type and single scattering albedo, *J. Geophys. Res.*, 115,  
649 D10209, doi:[10.1029/2009JD012697](https://doi.org/10.1029/2009JD012697), 2010.

650 di Sarra, A., Pace, G, Meloni, D., De Silvestri, L., Piacentino, S., and Monteleone, F.: Surface  
651 shortwave radiative forcing of different aerosol types in the Mediterranean, *Geophys. Res.*  
652 *Lett.*, 35, L02714, doi:[10.1029/2007GL032395](https://doi.org/10.1029/2007GL032395), 2008.

653 di Sarra, A., Di Biagio, C., Meloni, D., Monteleone, F., Pace, G., Pugnaghi, S., and Sferlazzo, D.:  
654        Shortwave and longwave radiative effects of the intense Saharan dust event of 25–26 March  
655        2010 at Lampedusa (Mediterranean Sea), *J. Geophys. Res.*, 116, D23209,  
656        doi:10.1029/2011JD016238, 2011.

657 Díaz, A. M., García, O.E., Díaz, J.P., Expósito, F.J., Utrillas, M.P., Martínez-Lozano, J.A., Alados-  
658        Arboledas, L., Olmo, F.J., Lorente, J., Cachorro, V., Horvath, H., Labajo, A., Sorribas, M.,  
659        Vilaplana, J.M., Silva, A.M., Elias, T., Pujadas, M., Rodrigues, J.A., and González, J.A.:  
660        Aerosol radiative forcing efficiency in the UV region over southeastern Mediterranean:  
661        VELETA2002 campaign, *J. Geophys. Res.*, 112, D06213, doi:10.1029/2006JD007348, 2007.

662 Dubovik, O., and King, M.D.: A flexible inversion algorithm for retrieval of aerosol optical  
663        properties from Sun and sky radiance measurements, *J. Geophys. Res.*, 105, 20673-20696,  
664        2000.

665 Dubovik, O., Smirnov, A., Holben, B.N., King, M.D., Kaufman, Y.J., Eck, T.F., and Slutsker, I.:  
666        Accuracy assessments of aerosol optical properties retrieved from Aerosol Robotic Network  
667        (AERONET) Sun and sky radiance measurements, *J. Geophys. Res.*, 105, 9791-9806, 2000.

668 Dubovik, O., Sinyuk, A., Lapyonok, T., Holben, B.N., Mishchenko, M., Yang, P., Eck, T.F.,  
669        Volten, H., Muñoz, O., Veihelmann, B., van der Zande, W.J., Leon, J.F., Sorokin, M., and  
670        Slutsker, I.: Application of spheroid models to account for aerosol particle nonsphericity in  
671        remote sensing of desert dust, *J. Geophys. Res.*, 111, D11208, 2006.

672 Esteve, A.R., Estellés, V., Utrillas, M.P., and Martínez-Lozano, J.A.: Analysis of the aerosol  
673        radiative forcing over a Mediterranean urban coastal site, *Atmos. Res.*, 137, 194-204,  
674        <http://dx.doi.org/10.1016/j.atmosres.2013.10.009>, 2014.

675 Foyo-Moreno, I., Alados, I., Antón, M., Fernández-Gálvez, J., Cazorla, A., and Alados-Arboledas,  
676 L.: Estimating aerosol characteristics from solar irradiance measurements at an urban location  
677 in Southeastern Spain, *J. Geophys. Res. Atmos.*, 119, 1845–1859, doi:10.1002/2013JD020599,  
678 2014.

679 García, O. E., Díaz, A. M., and Expósito, F. J.: Validation of AERONET estimates of atmospheric  
680 solar fluxes and aerosol radiative forcing by ground-based broadband measurements, *J.*  
681 *Geophys. Res.*, 113, D21207, doi:10.1029/2008JD010211, 2008.

682 García, R.D., García, O.E., Cuevas, E., Cachorro, V.E., Romero-Campos, P.M., Ramos, R., and de  
683 Frutos, A.M.: Solar radiation measurements compared to simulations at the BSRN Izaña  
684 station: Mineral dust radiative forcing and efficiency study, *J. Geophys. Res. Atmos.*, 119, 179–  
685 194, doi:10.1002/2013JD020301, 2014.

686 Gkikas, A., Hatzianastassiou, N., Mihalopoulos, N., Katsoulis, V., Kazadzis, S., Pey, J., Querol, X.,  
687 and Torres, O.: The regime of intense desert dust episodes in the Mediterranean based on  
688 contemporary satellite observations and ground measurements, *Atmos. Chem. Phys.*, 13,  
689 12135–12154, doi:10.5194/acp-13-12135-2013, 2013.

690 Guerrero-Rascado, J.L., Olmo, F. J., Avilés-Rodríguez, I., Navas-Guzmán, F., Pérez-Ramírez, D.,  
691 Lyamani, H., and Alados-Arboledas, L.: Extreme Saharan dust event over the southern Iberian  
692 Peninsula in September 2007: active and passive remote sensing from surface and Satellite,  
693 *Atmos. Chem. Phys.*, 9, 8453–8469, doi:10.5194/acp-9-8453-2009, 2009.

694 Gueymard, C.: The sun's total and spectral irradiance for solar energy applications and solar  
695 radiation models, *Sol. Energy*, 76, 423–453, 2004.

696 Hansen, J. E., Sato, M., Lacis, A., Ruedy, R., Tegen, I., and Matthews, E.: Climate forcings in the  
697 industrial era, *Proc. Natl. Acad. Sci. U.S.A.*, 95, 12753–12758, doi:10.1073/pnas.95.22.12753,  
698 1998.

699 Hatzianastassiou, N., Katsoulis, B., and Vardavas, I.: Global distribution of aerosol direct radiative  
700 forcing in the ultraviolet and visible arising under clear skies, *Tellus B*, 56, 51–71,  
701 doi:10.1111/j.1600-0889.2004.00085.x, 2004.

702 Hess, M., Koepke, P., and Schult, I.: Optical Properties of Aerosols and Clouds: The Software  
703 Package OPAC, *Bull. Am. Meteorol. Soc.*, 79, 831-844, 1998.

704 Holben, B.N., Eck, T.F., Slutsker, I., Tanré, D., Buis, J.P., Setzer, A., Vermote, E., Reagan, J.A.,  
705 KAufman, Y.J., Nakajima, T., Lavenu, F., Jankowiak, I., and Smirnov, A.: AERONET – A  
706 federated instrument network and data archive for aerosol characterization, *Rem. Sen. Environ.*,  
707 66, 1–16, 1998.

708 Horvath, H., Alados Arboledas, L., Olmo, F. J., Jovanovic, O., Gangl, M., Kaller, W., Sánchez, C.,  
709 Sauerzopf, H., and Seidl, S.: Optical characteristics of the aerosol in Spain and Austria and its  
710 effect on radiative forcing, *J. Geophys. Res.*, 107(D19), 4386, doi:10.1029/2001JD001472,  
711 2002.

712 Jayaraman, A., Lubin, D., Ramachandran, S., Ramanathan, V. , Woodbridge, E., Collins, W. D.,  
713 and Zalpuri, K. S.: Direct observations of aerosol radiative forcing over the tropical Indian  
714 Ocean during the Janauary–February 1996 pre-INDOEX cruise, *J. Geophys. Res.*, 103, 13,827–  
715 13,836, doi:10.1029/98JD00559, 1998.

716 Kazadzis, S., Kouremeti, N., Bais, A., Kazantzidis, A., and Meleti, C.: Aerosol forcing efficiency in  
717 the UVA region from spectral solar irradiance measurements at an urban environment, *Ann.*  
718 *Geophys.*, 27, 2515–2522, doi:10.5194/angeo-27-2515-2009, 2009.

719 Lucht, W. and Roujean, J.L.: Consideration in parametric modelling of BRDF and albedo from  
720 multi-angular satellite sensors observations, *Remote Sens. Rev.*, 18, 343–379, 2000.

721 Lyamani, H., Olmo, F.J., and Alados-Arboledas, L.: Saharan dust outbreak over southeastern Spain  
722 as detected by sun photometer, *Atmos. Env.*, 39, 7276-7284,  
723 doi:10.1016/j.atmosenv.2005.09.011, 2005.

724 Lyamani, H., Olmo, F. J., Alcántara, A., and Alados-Arboledas, L.: Atmospheric aerosols during  
725 the 2003 heat wave in southeastern Spain II: Microphysical columnar properties and radiative  
726 forcing, *Atmos. Environ.*, 40, 6465–6476, doi:10.1016/j.atmosenv.2006.04.047, 2006.

727 Mallet, M., Dubovik, O., Nabat, P., Dulac, F., Kahn, R., Sciare, J., Paronis, D., and Leon, J.F.:  
728 Absorption properties of Mediterranean aerosols obtained from multi-year ground-based  
729 remote sensing observations, *Atmos. Chem. Phys.*, 13, 9195-9210, doi:10.5194/acp-13-9195-  
730 2013, 2013.

731 Mateos, D., Antón, M., Valenzuela, A., Cazorla, A., Olmo, F.J., and Alados-Arboledas, L.: Short-  
732 wave radiative forcing at the surface for cloudy systems at a midlatitude site, *Tellus B*, 65,  
733 21069, <http://dx.doi.org/10.3402/tellusb.v65i0.21069>, 2013a.

734 Mateos, D., Antón, M., Sanchez-Lorenzo, A., Calbó, J., and Wild, M.: Long-term changes in the  
735 radiative effects of aerosols and clouds in a mid-latitude region (1985–2010), *Global Planet.  
736 Change*, 111, 288-295, <http://dx.doi.org/10.1016/j.gloplacha.2013.10.004>, 2013b.

737 Mateos, D., Sanchez-Lorenzo, A., Antón, M., Cachorro, V.E., Calbó, J., Costa, M.J., Torres, B., and  
738 Wild, M.: Quantifying the respective roles of aerosols and clouds in the strong brightening  
739 since the early 2000s over the Iberian Peninsula, *J. Geophys. Res. Atmos.*, 119, 10382–10393,  
740 doi:10.1002/2014JD022076, 2014.

741 Mayer, B., and Kylling, A.: Technical note: The libRadtran software package for radiative transfer  
742 calculations – description and examples of use, *Atmos. Chem.Phys.*, 5, 1855–1877, 2005.

743 Meloni, D., di Sarra, A., DeLuisi, J., Di Iorio, T., Fiocco, G., Junkerman, W., and Pace, G.:  
744 Tropospheric aerosols in the Mediterranean: 2. Radiative effects through model simulations and  
745 measurements, *J. Geophys. Res.*, 108(D10), 4317, doi:10.1029/2002JD002807, 2003.

746 Meloni, D., di Sarra, A., Di Iorio, T., and Fiocco, G.: Influence of the vertical profile of Saharan  
747 dust on the visible direct radiative forcing, *J. Quant. Spectrosc. Radiat. Transfer*, 93, 397–413,  
748 2005.

749 Moody, E.G., King, M.D., Platnick, S., Schaaf, C.B., and Gao, F.: Spatially complete global  
750 spectral surface albedos: value-added datasets derived from Terra MODIS land products, *IEEE*  
751 *T. Geosci. Remote.*, 43, 144–158, 2005.

752 Navas-Guzmán, F., Bravo-Aranda, J.A., Guerrero-Rascado, J.L., Granados-Muñoz, M.J., and  
753 Alados-Arboledas, L.: Statistical analysis of aerosol optical properties retrieved by Raman lidar  
754 over Southeastern Spain, *Tellus B*, 65, 21234, <http://dx.doi.org/10.3402/tellusb.v65i0.21234>,  
755 2013.

756 Nikitidou, E., Kazantzidis, A., De Bock, V., and De Backer, H.: The aerosol forcing efficiency in  
757 the UV region and the estimation of single scattering albedo at a typical West European site,  
758 *Atmos. Env.*, 69, 313-320, doi:<http://dx.doi.org/10.1016/j.atmosenv.2012.12.035>, 2013.

759 Obregón M.A., Pereira S, Wagner F, Serrano A, Cancillo ML, Silva AM.: Regional differences of  
760 column aerosol parameters in western Iberian Península, *Atmos. Environ.*, 62, 208-219, doi:  
761 10.1016/j.atmosenv.2012.08.016, 2012

762 Pace, G., di Sarra, A., Meloni, D., Piacentino, S., and Chamard, P.: Aerosol optical properties at  
763 Lampedusa (central Mediterranean): 1. Influence of transport and identification of different  
764 aerosol types, *Atmos. Chem. Phys.*, 6, 697–713, 2006.

765 Panicker, A. S., Pandithurai, G., Safai, P. D., and Kewat, S.: Observations of enhanced aerosol  
766 longwave radiative forcing over an urban environment, *Geophys. Res. Lett.*, 35, L04817,  
767 doi:10.1029/2007GL032879, 2008.

768 Pérez-Ramírez, D., Aceituno, J., Ruiz, B., Olmo, F.J., and Alados-Arboledas, L.: Development and  
769 calibration of a star photometer to measure the aerosol optical depth: Smoke observations at a  
770 high mountain site, *Atmos. Env.* 42(11), 2733–2738, 2008.

771 Pey, J., Querol, X., Alastuey, A., Forastiere, F, and Stafoggia, M. African dust outbreaks over the  
772 Mediterranean Basin during 2001–2011: PM<sub>10</sub> concentrations, phenomenology and trends, and  
773 its relation with synoptic and mesoscale meteorology, *Atmos. Chem. Phys.*, 13, 1395-1410,  
774 doi:10.5194/acp-13-1395-2013, 2013.

775 Prats, N., Cachorro, V.E., Berjón, A., Toledano, C., and De Frutos, A.M.: Column-integrated  
776 aerosol microphysical properties from AERONET Sun photometer over south-western Spain.  
777 *Atmos. Chem. Phys.* 11, 12353-12547, doi:10.5194/acpd-11-12353-2011, 2011.

778 Querol, X., Alastuey, A., Pandolfi, M., Reche, C., Pérez, N., Minguillón, M.C., Moreno, T., Viana,  
779 M., Escudero, M., Orio, A., Pallarés, M., and Reina, F.: 2001-2012 trends of air quality in  
780 Spain, *Sci. Total Environ.*, 490, 957-969, 2014.

781 Rajeev, K., and Ramanathan, V.: Direct observations of clear-sky aerosol radiative forcing from  
782 space during the Indian Ocean Experiment, *J. Geophys. Res.*, 106, 17,221–17,235,  
783 doi:10.1029/2000JD900723, 2001.

784 Reche, C., Viana, M., Moreno, T., Querol, X., Alastuey, A., Pey, J., Pandolfi, M., Prèvôt, A., Mohr,  
785 C., Richard, A., Artiñano, B., Gomez-Moreno, F.J., and Cots, N.: Peculiarities in atmospheric  
786 particle number and size-resolved speciation in an urban area in the western Mediterranean:  
787 Results from the DAURE campaign, *Atmos. Env.*, 45, 5282-5293,  
788 doi:10.1016/j.atmosenv.2011.06.059, 2011.

789 Román, R., Antón, M., Valenzuela, A., Gil, J.E., Lyamani, H., de Miguel, A., Olmo, F.J., Bilbao, J.,  
790 and Alados-Arboledas, L.: Evaluation of the desert dust effects on global, direct, and diffuse  
791 spectral ultraviolet irradiance, *Tellus B*, 65, 19578,  
792 <http://dx.doi.org/10.3402/tellusb.v65i0.19578>, 2013.

793 Román, R., Bilbao, J., and de Miguel, A.: Solar radiation simulations in the Iberian Peninsula:  
794 Accuracy and sensitivity to uncertainties in inputs of a radiative transfer model, *J. Quant.*  
795 *Spectrosc. Ra.*, 145, 95-109, 2014.

796 Ruckstuhl, C., Philipona, R., Behrens, K., Coen M.C., Dürr, B., Heimo, A., Mätzler, C., Nyeki, S.,  
797 Ohmura, A., Vuilleumier, L., Weller, M., Wehrli, C., and Zelenka, A.: Aerosol and cloud  
798 effects on solar brightening and the recent rapid warming, *Geophys. Res. Lett.*, 35, L12708,  
799 doi:10.1029/2008GL034228, 2008.

800 Saha, A., Mallet, M., Roger, J. C., Dubuisson, P., Piazzola, J., and Despiau, S.: One year  
801 measurements of aerosol optical properties over an urban coastal site: Effect on local direct  
802 radiative forcing, *Atmos. Res.*, 90, 195–202, doi:10.1016/j.atmosres.2008.02.003, 2008.

803 Sanchez-Lorenzo, A., Calbó, J., and Wild, M.: Global and diffuse solar radiation in Spain: Building  
804 a homogeneous dataset and assessing trends, *Global Planet. Change*, 100, 343-352,  
805 <http://dx.doi.org/10.1016/j.gloplacha.2012.11.010>, 2013.

806 Santos, D., Costa, M. J., and Silva, A. M.: Direct SW aerosol radiative forcing over Portugal,  
807 Atmos. Chem. Phys., 8, 5771–5786, doi:10.5194/acp-8-5771-2008, 2008.

808 Schuster, G. L., Dubovik, O., and Holben, B. N.: Angstrom exponent and bimodal aerosol size  
809 distributions, J. Geophys. Res., 111, D07207, doi:10.1029/2005JD006328, 2006.

810 Sen, P. K.: Estimates of the regression coefficient based on Kendall's tau, J. Am., Stat. Assoc., 63,  
811 1379–1389, 1968.

812 Shettle, E. P.: Models of aerosols, clouds and precipitation for atmospheric propagation studies,  
813 paper presented at Conference on Atmospheric Propagation in the UV, Visible, IR and MM-  
814 Region and Related System Aspects, NATO Adv. Group for Aerosp. Res. and Dev.,  
815 Copenhagen, 1989.

816 Stamnes, K., Tsay, S.C., Wiscombe, W., and Laszlo, I.: DISORT, a General-Purpose Fortran  
817 Program for Discrete-Ordinate-Method Radiative Transfer in Scattering and Emitting Layered  
818 Media: Documentation of Methodology, Tech. rep. Dept. of Physics and Engineering Physics,  
819 Stevens Institute of Technology, Hoboken, NJ 07030, 2000.

820 Steinbrecht, W., Köhler, U., Claude, H., Weber, M., Burrows, J.P., and van der A, R.J.: Very high  
821 ozone columns at northern mid-latitudes in 2010, Geophys Res Lett, 38, L06803,  
822 doi:10.1029/2010GL046634, 2011.

823 Toledano, C., Cachorro, V.E., Berjon, A., de Frutos, A.M., Sorribas, M., de la Morena, B., and  
824 Goloub, P.: Aerosol optical depth and Ångström exponent climatology at El Arenosillo  
825 AERONET site (Huelva, Spain), Q. J. R. Meterol. Soc., 133, 795-807, 2007a.

826 Toledano, C., Cachorro, V.E., de Frutos, A.M., Sorribas, M., Prats, N., and de la Morena, B.:  
827 Inventory of African desert dust events over the southwestern Iberian Peninsula in 2000-2005

828 with an AERONET Cimel Sun photometer, *J. Geophys. Res.* 112, doi:10.1029/2006JD008307,  
829 2007b.

830 Valenzuela, A., Olmo, F.J., Lyamani, H., Antón, M., Quirantes, A., and Alados-Arboledas, L.:  
831 Aerosol radiative forcing during African desert dust events (2005-2010) over Southeastern  
832 Spain, *Atmos. Chem. Phys.* 12, 10331–10351, doi:10.5194/acp-12-10331-2012, 2012.

833 Zhou, M., Yu, H., Dickinson, R. E., Dubovik, O., and Holben, B. N.: A normalized description of  
834 the direct effect of key aerosol types on solar radiation as estimated from Aerosol Robotic  
835 Network aerosols and Moderate Resolution Imaging Spectroradiometer albedos, *J. Geophys.*  
836 *Res.*, 110, D19202, doi:10.1029/2005JD005909, 2005.

837

Station	Latitude (°N)	Longitude (°E)	Altitude a.s.l. (m)	Time interval
Palencia	41.99	-4.52	750	2003-2012
Barcelona	41.39	2.12	125	2004-2012
Cabo da Roca	38.78	-9.50	140	2003-2011
Évora	38.57	-7.91	293	2005-2012
Granada	37.16	-3.61	680	2004-2012
El Arenosillo	37.11	-6.73	0	2000-2009

845 **Table 2.** Summary of AERONET data used for ARE calculations: aerosol optical depth (AOD),  
 846 single scattering albedo (SSA), asymmetry factor (g), precipitable water vapor column (PWC).  
 847 Estimated absolute uncertainty of AOD and SSA is given according to Dubovik et al. (2002), and  
 848 PWC error from Holben et al. (1998).

	AERONET database	Estimated uncertainty
AOD	Level 2.0	±0.01-0.02
SSA, g (AOD <sub>440</sub> >0.4)	Level 2.0	±0.03 (in SSA)
SSA, g (0.15<AOD <sub>440</sub> <0.4)	Level 1.5-filtered*	±0.05-0.07(in SSA)
SSA, g (AOD <sub>440</sub> <0.15)	Fixed value	
PWC	Level 2.0	10-15%

849 \*Filters applied are the same as in level 2.0 except for AOD<sub>440</sub> (see text).

854 **Table 3.** AFE values and their standard error for the UV, VIS, NIR, and SW ranges for, separately,  
 855 four SSA and three  $\alpha$  intervals over the Iberian Peninsula. Units are  $\text{Wm}^{-2}\tau^{-1}$ . SSA groups:  $0.85 \geq$   
 856  $\text{SSA}_1 > 0.80$  (group 1),  $0.90 \geq \text{SSA}_2 > 0.85$  (group 2),  $0.95 \geq \text{SSA}_3 > 0.90$  (group 3), and  $1.0 \geq$   
 857  $\text{SSA}_4 > 0.95$  (group 4); and  $\alpha$  groups:  $0 \leq \alpha_1 \leq 1$  (group 1),  $1.0 \leq \alpha_2 \leq 1.5$  (group 2), and  $1.5 < \alpha_3 \leq 2$   
 858 (group 3). The average values without any classification are also presented.

Variable	Group	AFE <sub>UV</sub>	AFE <sub>VIS</sub>	AFE <sub>NIR</sub>	AFE <sub>SW</sub>
$\alpha$	1	-5.41 ± 0.06	-30.1 ± 0.3	-20.9 ± 0.2	-56.5 ± 0.5
	2	-6.60 ± 0.09	-38.3 ± 0.4	-19.1 ± 0.2	-64.0 ± 0.6
	3	-7.06 ± 0.10	-39.4 ± 0.4	-16.9 ± 0.2	-63.3 ± 0.7
SSA	1	-9.7 ± 0.2	-52.8 ± 0.8	-24.9 ± 0.5	-87.4 ± 1.4
	2	-8.19 ± 0.10	-44.6 ± 0.4	-21.2 ± 0.2	-74.0 ± 0.6
	3	-6.37 ± 0.05	-35.9 ± 0.2	-19.5 ± 0.2	-61.8 ± 0.3
	4	-4.59 ± 0.05	-26.6 ± 0.2	-18.1 ± 0.2	-49.3 ± 0.3
Average		-5.98 ± 0.05	-33.7 ± 0.2	-19.34 ± 0.11	-59.1 ± 0.3

862 **Table 4.** Daily Forcing Efficiencies at the surface by previous studies. Legend: desert dust (DD),  
 863 continental-biomass burning (C-BB), and forest fires (FF).

864

Reference	Aerosol Type	AFE <sub>X</sub>	Value (Wm <sup>-2</sup> τ <sup>-1</sup> )	Time period	Region	More info.
Díaz et al. (2007)	Mixed	AFE <sub>UV</sub>	-3	July 2002	Spain	290-363 nm
Meloni et al. (2005)	DD Mixed	AFE <sub>VIS</sub>	-28.4 -45.6	July 2002	Central Mediterranean	
Lyamani et al. (2006)	Mixed	AFE <sub>VIS</sub>	-75.8	August 2003	Spain	2003 heat wave
Di Biagio et al. (2010)	DD C-BB Mixed	AFE <sub>SW</sub>	-68.9 -59.0 -94.9	2004-2007	Central Mediterranean	At the equinox
Esteve et al. (2014)	Mixed	AFE <sub>SW</sub>	-139.0	2003-2011	Spain	200 cloud-free days
Santos et al. (2008)	FF	AFE <sub>SW</sub>	-113.0	2004-2005	Portugal	Absorbing aerosols
di Sarra et al. (2011)	DD	AFE <sub>SW</sub>	-55	25-26/03/2010	Central Mediterranean	Strong event
García et al. (2014)	DD	AFE <sub>SW</sub>	-59	2009-2012	Canary Islands	386 cloud-free days
Costa et al. (2006)	DD	AFE <sub>SW</sub>	-116.9	7/04/2000	Korea	SSA = 0.76
Zhou et al. (2005)	DD	AFE <sub>SW</sub>	-80/-48	Monthly aerosol climatology	North Africa and Arabian Peninsula	Depending on surface albedo
Saha et al. (2008)	C-BB Mixed	AFE <sub>SW</sub>	-97.6 -81.5	2005-2006	French Mediterranean	0.7 < SSA < 0.8
Valenzuela et al. (2012)	DD	AFE <sub>SW</sub>	-70	2005-2010	Spain	

865

866

867

868

869 **Table A1.** Mean relative difference (RD) in the UV, VIS, NIR, and SW net fluxes if SSA = 0.90  
 870 and g = 0.75 are compared with different SSA and g scenarios for different SZA values.

871

SZA	RD <sub>UV</sub> (%)	RD <sub>VIS</sub> (%)	RD <sub>NIR</sub> (%)	RD <sub>SW</sub> (%)
30	±3.4	±1.9	±0.9	±1.5
60	±4.9	±3.0	±1.5	±2.4

872

873

874 Figure Captions

875 **Figure 1.** Annual cycle of daily values of AOD at 440 nm by box whisker plots for the six sites  
876 studied. Triangles and horizontal solid lines indicate the monthly average and median values,  
877 respectively.

878 **Figure 2.** Annual cycle of daily values of  $\alpha$  ('alpha' in the figure) by box whisker plots for the six  
879 sites studied. Triangles and horizontal solid lines indicate the monthly average and median values,  
880 respectively.

881 **Figure 3.** Relative frequency of aerosol type occurrence: maritime (MA), desert dust (DD),  
882 continental clean (CC), and continental polluted (CP) for the six sites studied.

883 **Figure 4.** Yearly values of  $AOD_{440nm}$  at the six sites: Barcelona (blue diamonds), Palencia (purple  
884 triangles), Évora (red squares), Cabo da Roca (grey crosses), Granada (black stars), and El  
885 Arenosillo (green circles). The text points out the statistically significant trend obtained. Vertical  
886 bars indicate the standard deviation of each yearly value at Barcelona station. The larger the  
887 symbols, the larger amount of data number that year (e.g., the smallest symbols indicate cases  
888 between 100 and 150 points, while the largest symbols show years with  $>250$  points).

889 **Figure 5.** Evolution of yearly  $ARE_{UV}$  (a),  $ARE_{VIS}$  (b),  $ARE_{NIR}$  (c), and  $ARE_{SW}$  (d) at the six sites:  
890 Barcelona (blue diamonds), Palencia (purple triangles), Évora (red squares), Cabo da Roca (grey  
891 crosses), Granada (black stars), and El Arenosillo (green circles). Vertical bars indicate the standard  
892 deviation of each yearly value at Palencia station.

893 **Figure 6.** Evolution of annual ARE at the four spectral ranges ( $ARE_{UV}$  purple diamonds,  $ARE_{VIS}$   
894 red squares,  $ARE_{NIR}$  green triangles, and  $ARE_{SW}$  black circles) and AOD at 500 nm (blue stars)  
895 averaging the data from the six Iberian ground-based sites (only years with at least three sites  
896 considered). Dashed lines point out the linear trends (see text).

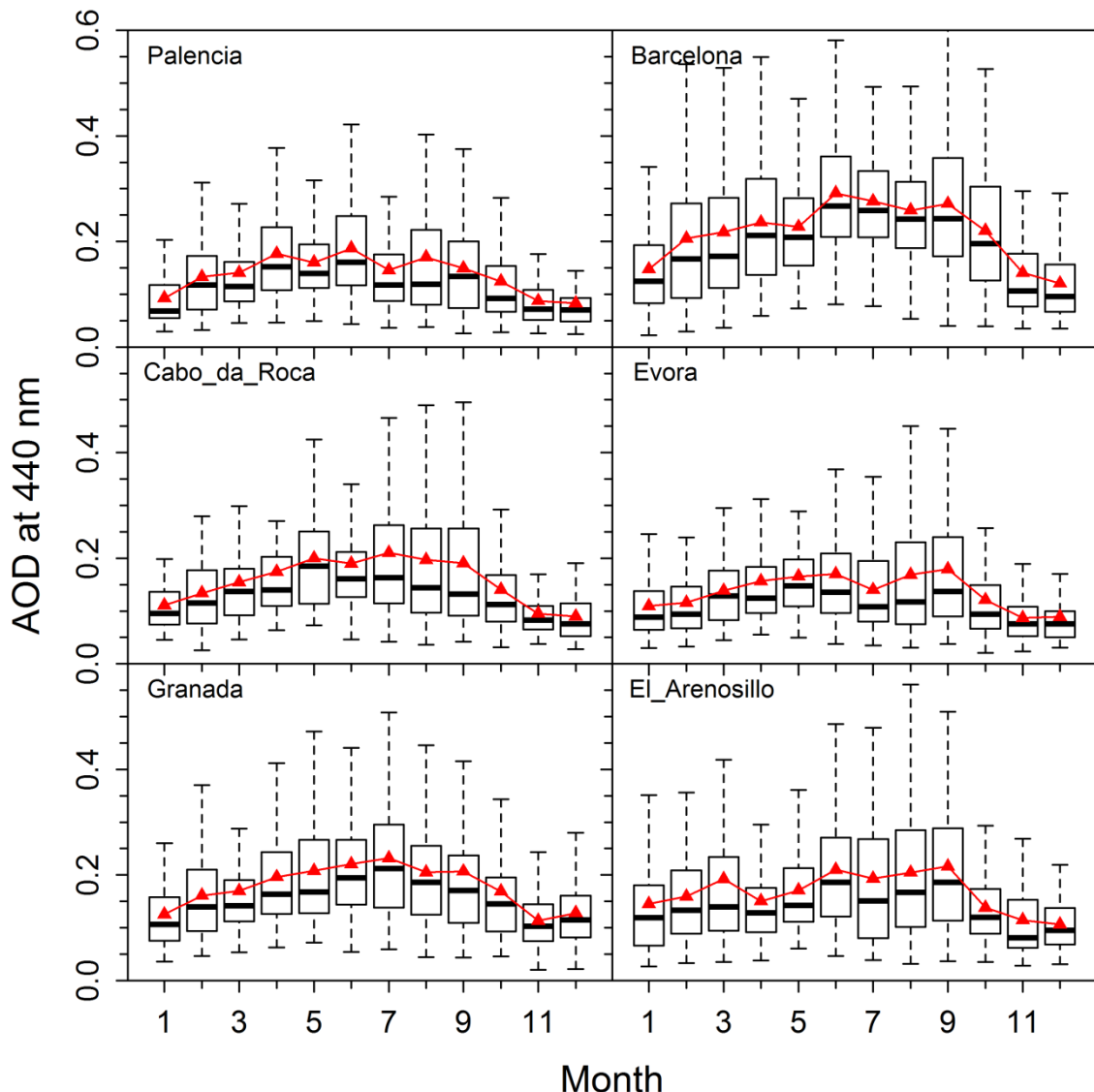
897 **Figure 7.** Annual cycle of  $ARE_{UV}$  (a),  $ARE_{VIS}$  (b),  $ARE_{NIR}$  (c), and  $ARE_{SW}$  (d) at the six sites:  
898 Barcelona (blue diamonds), Palencia (purple triangles), Évora (red squares), Cabo da Roca (grey  
899 crosses), Granada (black stars), and El Arenosillo (green circles). Vertical bars point out the  
900 standard deviation of each monthly value at Évora station.

901 **Figure 8.**  $AFE_{UV}$ ,  $AFE_{VIS}$ ,  $AFE_{NIR}$ , and  $AFE_{SW}$  against four groups of aerosol single scattering  
902 albedo and three intervals of  $\alpha$  at the six sites: Barcelona (blue diamonds), Palencia (purple  
903 triangles), Évora (red squares), Cabo da Roca (grey crosses), Granada (black stars), and El  
904 Arenosillo (green circles).

905 **Figure 9.** Dependence of  $AFE_{VIS}/AFE_{SW}$  (a, c, e) and  $AFE_{NIR}/AFE_{SW}$  (b, d, f) ratios on SSA for  
906 large,  $0 < \alpha < 1$  (a, b), medium,  $1 < \alpha < 1.5$  (c, d), and small,  $1.5 < \alpha < 2$  (e, f), particles at the six  
907 sites: Barcelona (blue diamonds), Palencia (purple triangles), Évora (red squares), Cabo da Roca  
908 (grey crosses), Granada (black stars), and El Arenosillo (green circles).

909

910 Figure 1

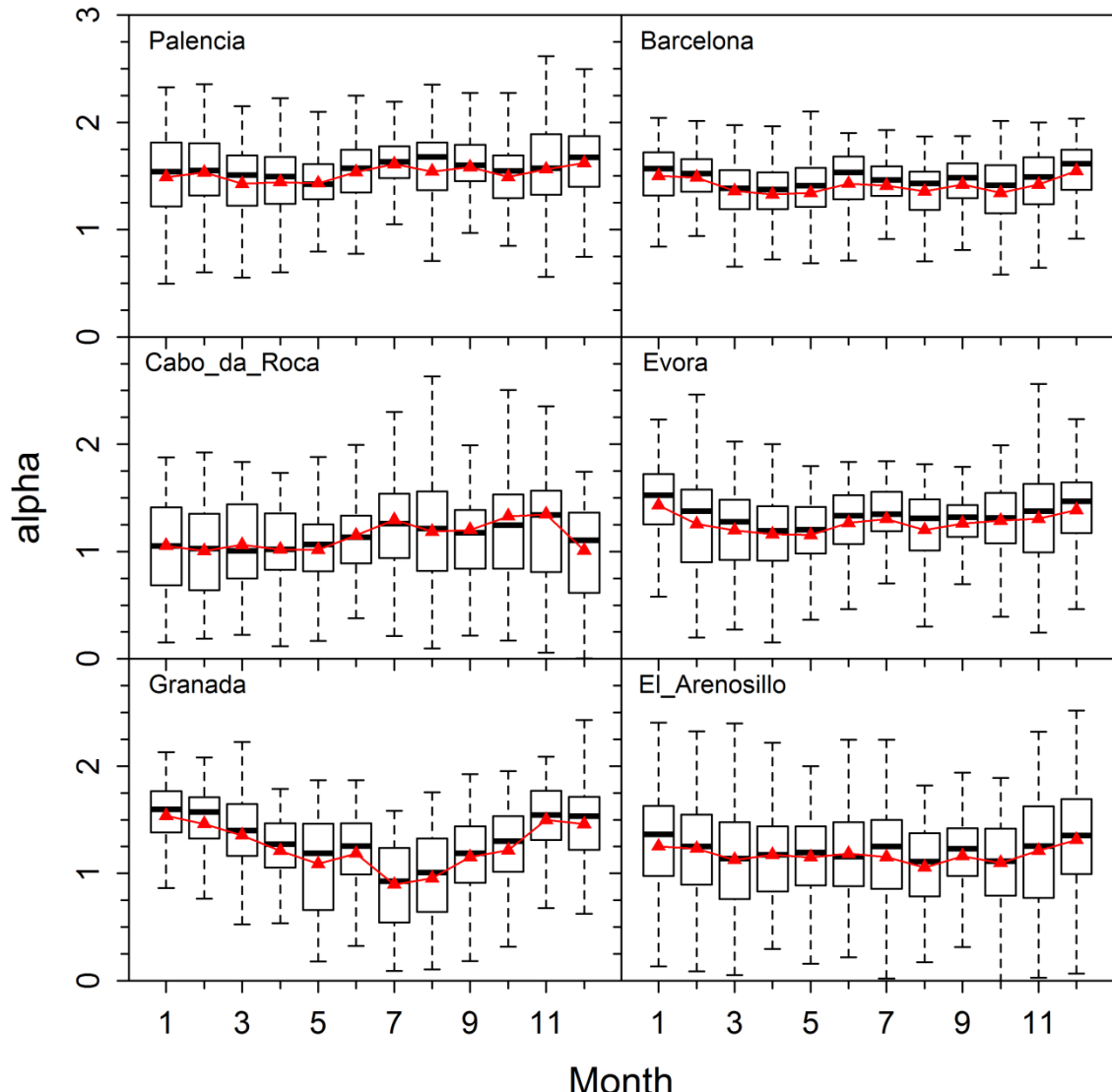


911

912 **Figure 1.** Annual cycle of daily values of AOD at 440 nm by box whisker plots for the six sites  
913 studied. Triangles and horizontal solid lines indicate the monthly average and median values,  
914 respectively.

915

916 Figure 2



917

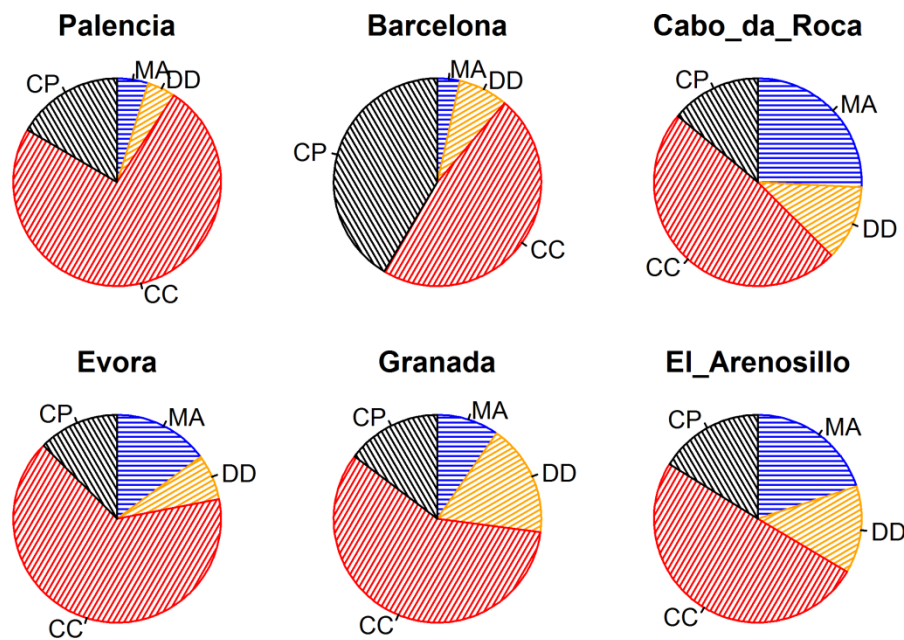
918 **Figure 2.** Annual cycle of daily values of  $\alpha$  ('alpha' in the figure) by box whisker plots for the six  
919 sites studied. Triangles and horizontal solid lines indicate the monthly average and median values,  
920 respectively.

921

922

923 Figure 3

924



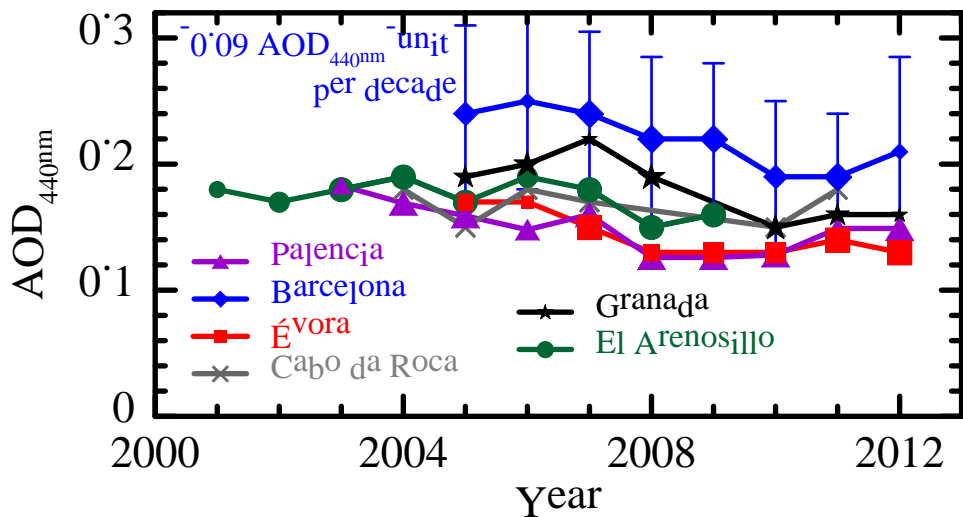
925

926 **Figure 3.** Relative frequency of aerosol type occurrence: maritime (MA), desert dust (DD),  
927 continental clean (CC), and continental polluted (CP) for the six sites studied.

928

929 Figure 4

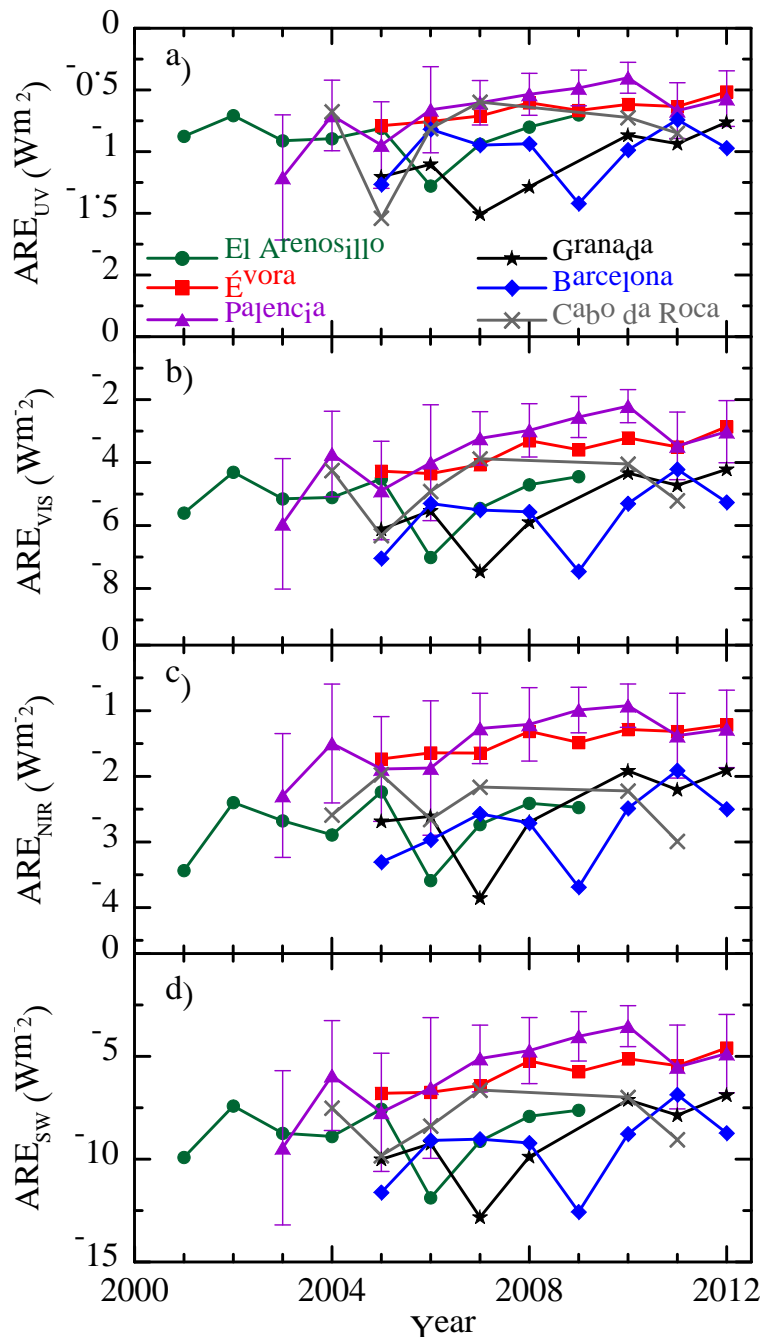
930



931

932 **Figure 4.** Yearly values of AOD<sub>440nm</sub> at the six sites: Barcelona (blue diamonds), Palencia (purple  
933 triangles), Évora (red squares), Cabo da Roca (grey crosses), Granada (black stars), and El  
934 Arenosillo (green circles). The text points out the statistically significant trend obtained. Vertical  
935 bars indicate the standard deviation of each yearly value at Barcelona station. The larger the  
936 symbols, the larger amount of data number that year (e.g., the smallest symbols indicate cases  
937 between 100 and 150 points, while the largest symbols show years with >250 points).

938

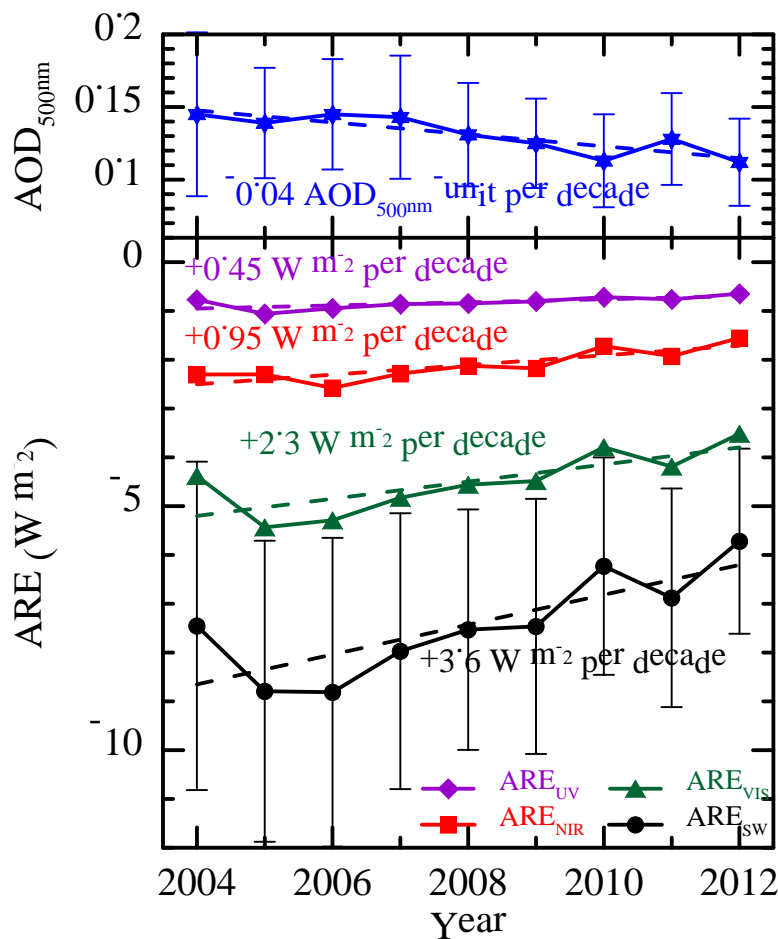


941 **Figure 5.** Evolution of yearly ARE<sub>UV</sub> (a), ARE<sub>VIS</sub> (b), ARE<sub>NIR</sub> (c), and ARE<sub>SW</sub> (d) at the six sites:  
942 Barcelona (blue diamonds), Palencia (purple triangles), Évora (red squares), Cabo da Roca (grey  
943 crosses), Granada (black stars), and El Arenosillo (green circles). Vertical bars indicate the standard  
944 deviation of each yearly value at Palencia station.

945 Figure 6

946

947



948

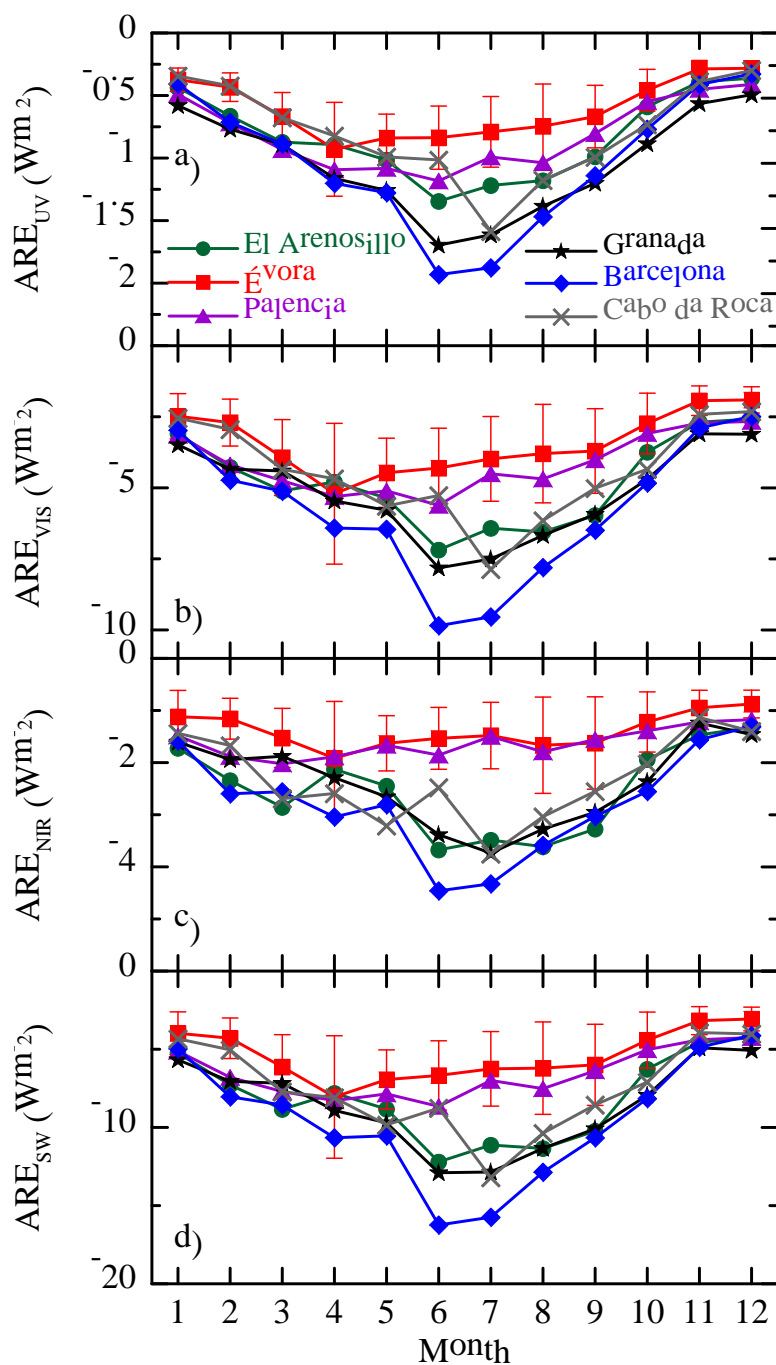
949

950 **Figure 6.** Evolution of annual ARE at the four spectral ranges (ARE<sub>UV</sub> purple diamonds, ARE<sub>VIS</sub>  
 951 red squares, ARE<sub>NIR</sub> green triangles, and ARE<sub>SW</sub> black circles) and AOD at 500 nm (blue stars)  
 952 averaging the data from the six Iberian ground-based sites (only years with, at least, three sites are  
 953 considered). Dashed lines point out the linear trends (see text). Vertical bars indicate the standard  
 954 deviation.

955

956 Figure 7

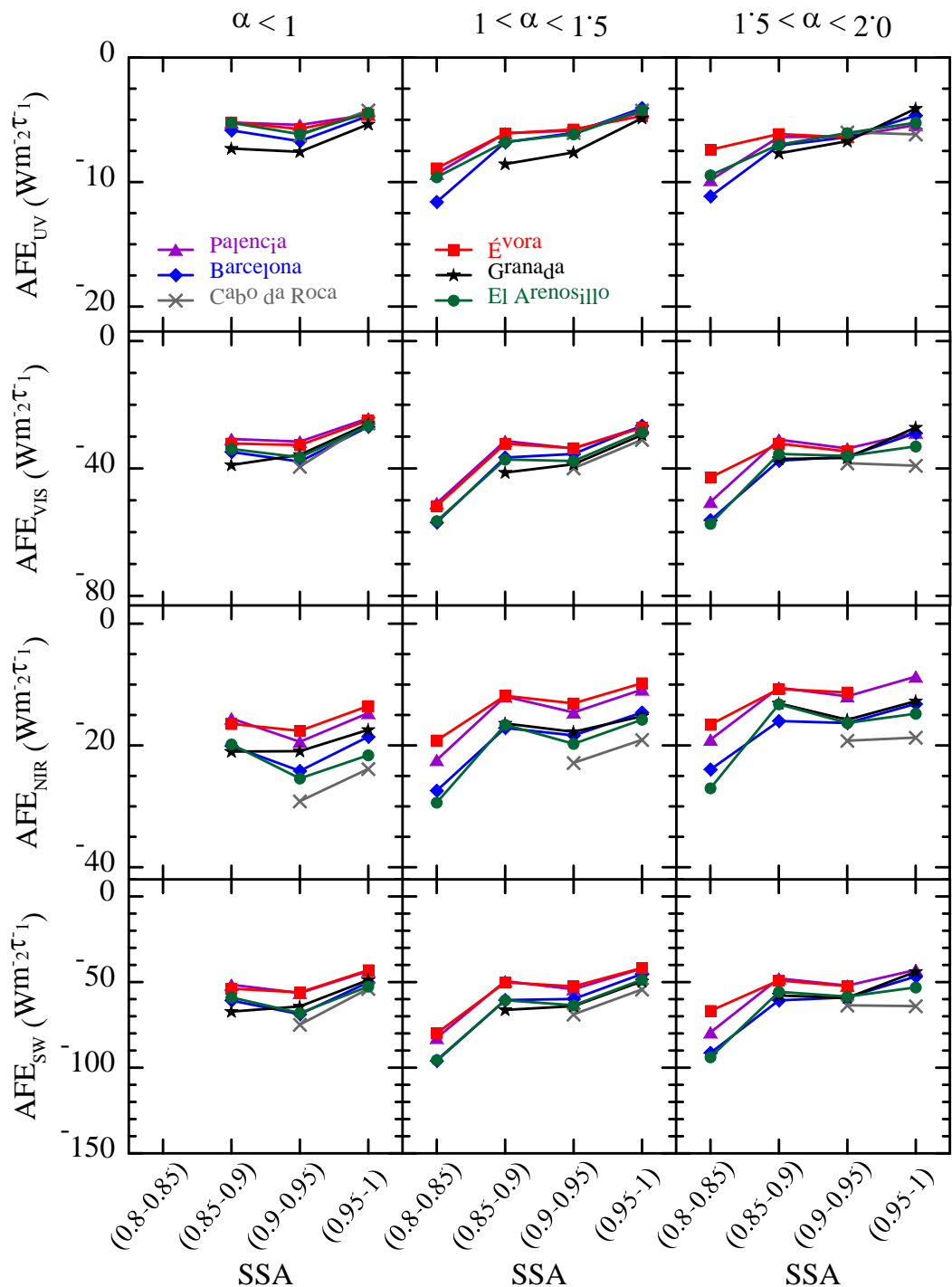
957



958

959 **Figure 7.** Annual cycle of ARE<sub>UV</sub> (a), ARE<sub>VIS</sub> (b), ARE<sub>NIR</sub> (c), and ARE<sub>SW</sub> (d) at the six sites:  
 960 Barcelona (blue diamonds), Palencia (purple triangles), Évora (red squares), Cabo da Roca (grey  
 961 crosses), Granada (black stars), and El Arenosillo (green circles). Vertical bars point out the  
 962 standard deviation of each monthly value at Évora station.

963 Figure 8

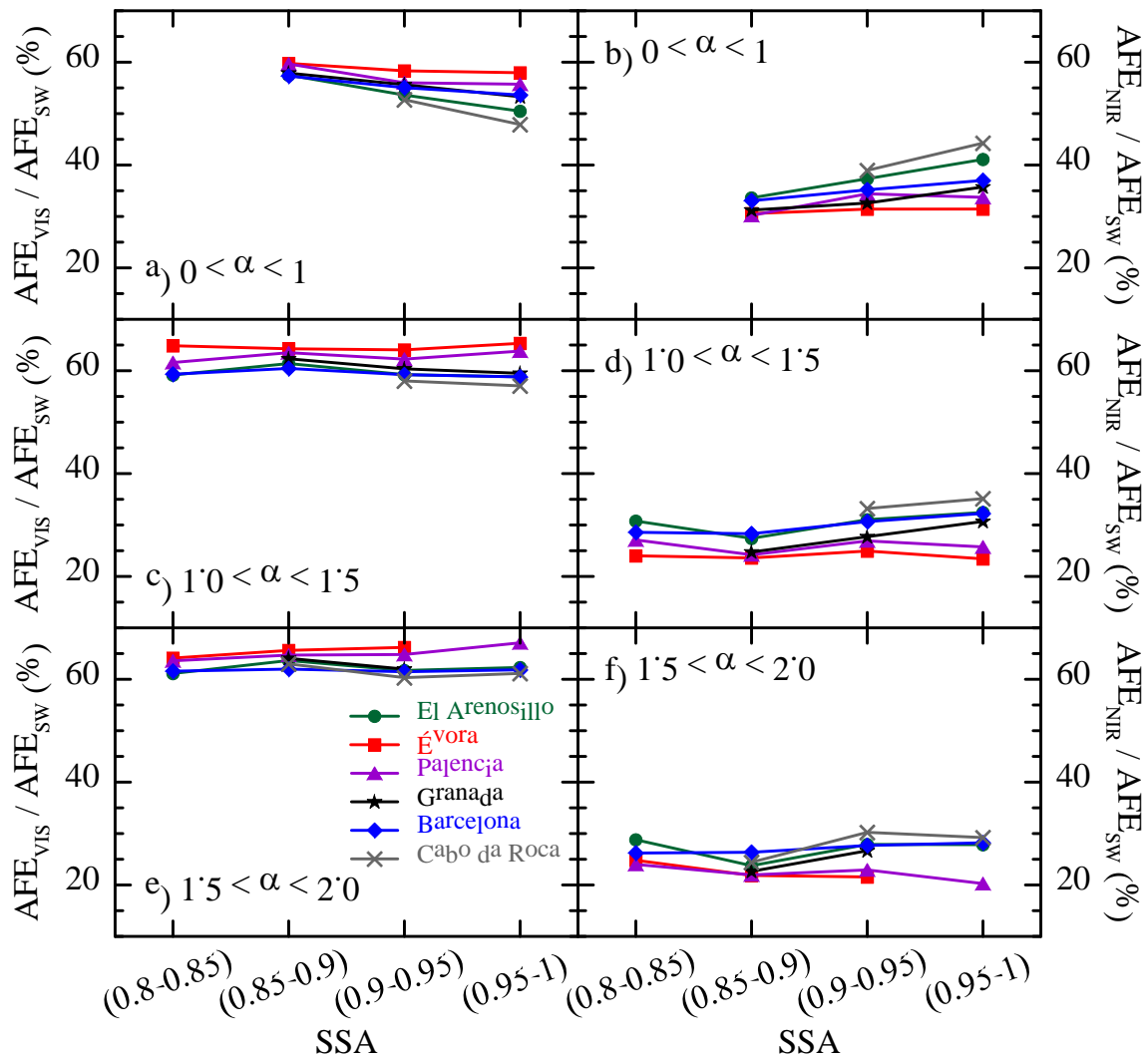


964

965 **Figure 8.** AFE<sub>UV</sub>, AFE<sub>VIS</sub>, AFE<sub>NIR</sub>, and AFE<sub>SW</sub> against four groups of aerosol single scattering  
 966 albedo and three intervals of  $\alpha$  at the six sites: Barcelona (blue diamonds), Palencia (purple  
 967 triangles), Évora (red squares), Cabo da Roca (grey crosses), Granada (black stars), and El  
 968 Arenosillo (green circles).

969 Figure 9

970



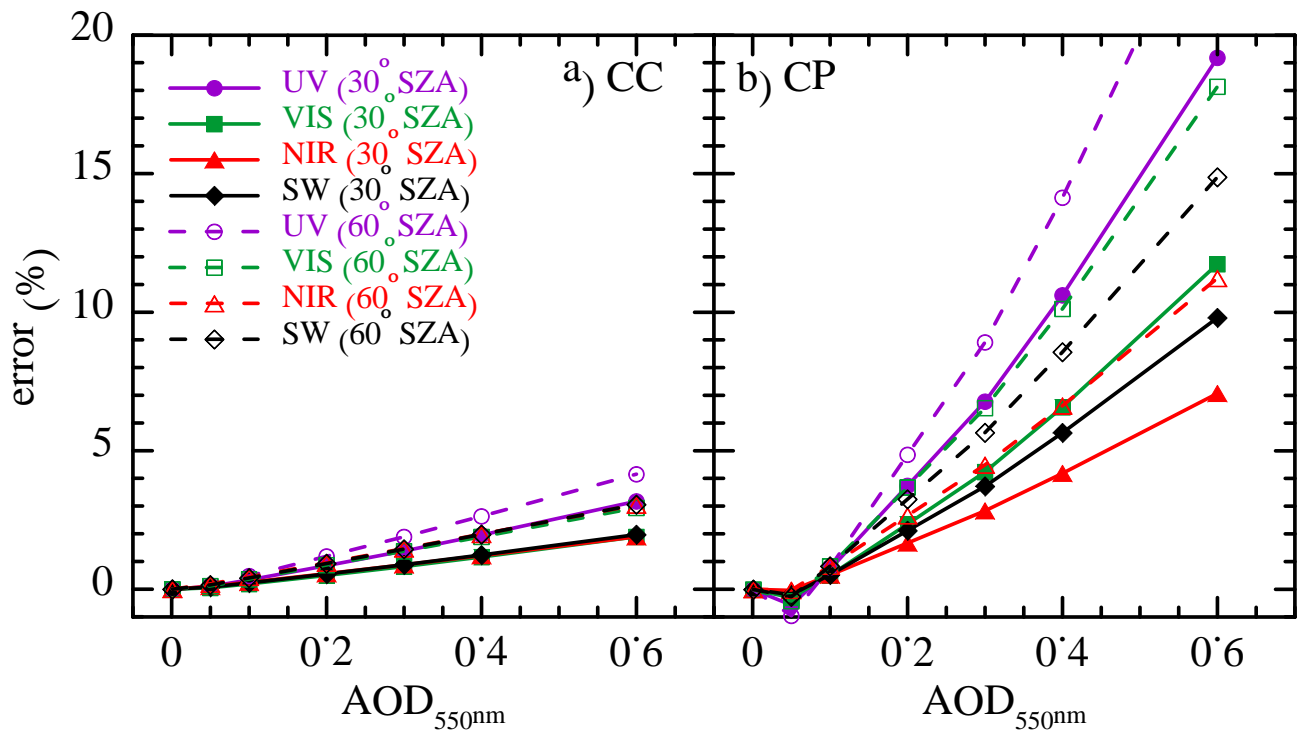
971

972 **Figure 9.** Dependence of AFE<sub>VIS</sub>/AFE<sub>SW</sub> (a, c, e) and AFE<sub>NIR</sub>/AFE<sub>SW</sub> (b, d, f) ratios on SSA for  
973 large,  $0 < \alpha < 1$  (a, b), medium,  $1 < \alpha < 1.5$  (c, d), and small,  $1.5 < \alpha < 2$  (e, f), particles at the six  
974 sites: Barcelona (blue diamonds), Palencia (purple triangles), Évora (red squares), Cabo da Roca  
975 (grey crosses), Granada (black stars), and El Arenosillo (green circles).

976

977 Figure A1

978



979

980 Figure A1. Dependence on aerosol load of the error committed when the optical properties are fixed  
981 in the different spectral ranges for two SZAs ( $30^\circ$  solid lines and symbols, and  $60^\circ$  dashed lines and  
982 open symbols), and (a) continental clean (CC) and (b) continental polluted (CP) aerosols.

983